Spatial exploration of immune cell heterogeneity in skin functional scar-less wound regeneration model at single-cell resolution

Yang Yang[a#], Chenyu Chu[a#], Chen Hu[a], Chenbing Wang[a], Shengan Rung[a], Yili Qu[a*], Yi Man[a*]

[a] Department of Oral Implantology &State Key Laboratory of Oral Diseases & National Clinical Research Center for Oral Diseases, West China Hospital of Stomatology, Sichuan University, Chengdu 610041, China.

 # These authors contributed equally to this work

** Corresponding to Yi Man, E-mail: manyi780203@126.com and Yili Qu, E-mail: qqyili@126.com*

Corresponding author:

Yi Man, DDS, Ph.D

Professor and Chair

Department of Oral Implantology, West China Hospital of Stomatology, Sichuan University, 14#, 3rd section, Renmin South Road

Chengdu 610041, China

Tel: 0086-28-85503571

E-mail: manyi780203@126.com

Yili Qu, DDS, Ph.D

Associate Professor

State Key Laboratory of Oral Diseases, West China Hospital of Stomatology, Sichuan University, 14#, 3rd section, Renmin South Road

Chengdu 610041, China

Tel: 0086-28-85503571

E-mail: qqyili@126.com

Abstract

Fibrotic scar is one of the primary impediments to severe skin wound healing, characterized by excessive deposition of extracellular matrix (ECM) devoid of skin appendages including hair follicle (HF). Intriguingly, functional hair follicles can regenerate specifically in the large wound center of adult mice, termed wound-induced hair neogenesis (WIHN). Single-cell RNA sequencing (scRNA-Seq) comparisons of small and large wound showed increased activation of adaptive immune systems which might associated with predominance of papillary fibroblast (PF) in large wound. Integration the gene expression profiles of spatial transcriptomic (ST) and scRNA-Seq highlighted a “pro-regenerative” immune niche, composing of T cells, pro-inflammatory macrophage (PIM) and monocyte surrounding the migrating hair follicle stem cell (HFSC) and PF in large wound center. Local pro-regenerative immune response predicted by Cellchat provided potential therapeutic target for the further HF regeneration. Aligned electrospinning scaffolds were previously shown to accelerate small wound healing with the immunomodulatory effect of T cells and macrophages. Here we showed that wound recapitulated normal skin architecture with the implantation of scaffold despite wound size. Enlarged distribution of the “pro-regenerative” immune niche co-localization with PF may account for the well-proportioned de novo

HF in scaffold-implanted group. Collectively, our study illustrated that manipulating the adaptive immune system may stimulate de novo HF regeneration via local cell-cell interactions.

Keywords

Wound-induced hair follicle neogenesis; Immune microenvironment; Immunomodulatory; Tissue engineering; Single-cell RNA-Seq; Spatial transcriptomics

Introduction

Following severe skin injury, skin wounds in adult generally heal by fibrotic scarring. Unlike uninjured normal skin which contain "basket-weave" pattern extracellular matrix (ECM) studded with dermal appendages such as hair follicle (HF) and sebaceous gland (SG), scar tissue owned a denser and parallel collagen fibers devoid of HF regeneration. Lack normal skin's function, flexibility, and aesthetics as the result of absent functional appendages, scar formation is one of the primary impediments to skin wound healing[1]. When such dysfunctional repairs of skin are small, they may not become a significant problem. But large lifelong scar can seriously affect the patient's daily life[2]. Intriguingly, some capacity for "half-functional" regeneration has been demonstrated in large (larger than 1 cm^2) full thickness wound of adult mice skin. De novo HFs and adipocytes can regenerate specifically in wound center, termed wound-induced hair neogenesis (WIHN)[3].The

actively growing HFs in wound center are critical for myofibroblast-to-adipocyte reprogramming, which is helpful to reduce excessive ECM deposition around de novo HFs[4].Curiously, the underlying mechanism that WIHNs are limited to the large wound center remains unclear, which makes it as an interesting model to explore the secret of perfect skin regeneration. In fact, WIHN is restricted by space as well as time. De novo HFs appear within a narrow window of time, which matches the activation period of immune system. Generally, proliferation phase (re-epithelialization, granulation tissue formation) starts at 1week post wound, and the influx of immune cells into the wound also reaches its peak[5]. After wound healing, inflammatory responses decreased, along with disappearance regeneration signals. It has been inferred that immune cells (mainly macrophages, T cells) are the key orchestrators of wound healing that selectively promoting scarring[6,7] or regenerative WIHN[8-11]. Collectively, these findings indicate that the impact of immune system in response to wound remains incompletely understood. Unrevealing the spatiotemporal heterogeneity of immune cells between the scar or WIHN model might be a fascinating way to understand the mechanism of functional wound regeneration. Along with deeper understanding of biological process and emergence of mature engineering techniques, there are growing possibility for well-designed biosynthetic materials to achieve specific therapeutic

goals[12]. Biological cues can be integrated into polymer scaffold to create a mimic of the native ECM, which is the framework guiding the activity of immune cells[13,14]. Formation of a pro-regenerative immune microenvironment might support the development of proper functional skin regeneration instead of fibrotic scar[15]. Our previous study has showed that the aligned topography electrospinning scaffold was able to lead to an enhanced regeneration of HF (small wound, diameter 6mm), along with the immunomodulatory effect of activating the adaptive system[16]. On this basis, we next found that aligned scaffold with 300nm diameter has a better pro-regenerative effect (small wound, diameter 6mm), along with the recruitment of reparative macrophages [17]. However, we wonder if ECM scaffold could exert the regenerative effect in mouse large wounds either. To sum up, there still some elusive questions to be solved: (1) Spatial heterogeneity of immune-microenvironment between small wound, large wound margin, and large wound center;(2) Whether the biosynthetic ECM scaffold exerts the further pro-regenerative effect when implanted in the large wound, and the underlying immune-regulatory mechanism;(3) Is there still any difference of immune microenvironment between small and large wound with implanted scaffold? To answer the question above, here we integrated the high-dimensional multiomics approaches including bulk-tissue RNA sequencing (bulk-seq), single-cell RNA sequencing

(scRNA-seq), and spatial transcriptomics (ST) to delineate the delicate spatial characteristics of immune-microenvironment in different wound size with/without implanted scaffold. Integration of scRNA-seq and ST profiles highlighted a “pro-regenerative” niche composed of T cells, pro-inflammatory macrophage (PIM) and monocyte in the large wound center, as well as whole wound around implanted ECM scaffold. Those immune cells were co-localized with papillary fibroblast (PF), which is the precursor of HF[18] . There were abundant intercellular communications between PF and the immune cells mentioned above, which provide the promising therapy target for the functional wound regeneration in the future.

Result

WIHN occurs in large wound center with activation of adaptive immune system

We respectively created full-thickness small wound (Ctrl_SW, diameter=0.6cm) and large wound (Ctrl_LW, diameter =1.5cm) in mice loose dorsal skin. To mimic the healing model of human’s tight skin, silicone splints were sutured with the wound margin to minimize the contraction of mice’s panniculus carnosus in response to wounding[19] (Fig. 1, A and B). Comparison of Ctrl_SW and Ctrl_LW group during the remodeling phase (POD 28) confirmed that small wounds healing with the characteristic of fibrotic scar: excessive dense, parallel collagen

deposition without dermal appendages. While de novo hair follicles could regenerate in large wound center, suggesting an “half-regenerative” micro-environment (Fig. 1C). To ask whether this regenerative capacity correlated with immune response, we compared Ctrl_SW and Ctrl_LW groups for bulk-RNA transcription on POD7, a time point of both tissue proliferation and immune cell recruitment. In comparison with small wound, the large wound showed up-regulated gene expression in Gene Ontology (GO) terms including hair follicle development and αβT cell differentiation, and Kyoto Encyclopedia of Genes and Genomes (KEGG) pathways including Wnt signaling pathway and Th17 cell differentiation pathway (Fig. 1D). Volcano plots showed that genes related to adaptive immune responses were significantly up regulated in Ctrl_LW group, including genes (Lef1, Shh) which had been convinced to be correlated with HF regeneration[20-22] (Fig. 1E). Correlation heatmap showed the positive correlation between HF regeneration related genes and adaptive immune response related genes among 6 samples (Fig. 1 F). Immunofluorescent (IF) and immunohistochemistry (IHC) staining for Cd3 confirmed that large wound center maintained substantial adaptive T cell infiltration on POD 7 (Fig. 1G).

scRNA-seq revealed higher proportion of PF and HFP from Ctrl_LW group

Next, we undertook single-cell RNA sequencing (Sc RNA-seq) to

compare the transcriptional profiling between Ctrl_SW and Ctrl_LW group at single-cell resolution (Fig. S1A). After quality control, 18,621 cell were included in the final dataset (11,217 from the Ctrl_LW group and 7,404 from the Ctrl_SW group). We firstly categorized the cells into 10 main clusters based on gene expression profiles using Seurat, and the proportion of cells from two groups were shown in Fig. S1B. Top (based on average |log2FC| value) marker genes for each cell cluster were shown in the Fig. S1C. Firstly, we extracted cells defined as fibroblast (consisting of dermal papilla cells and wound fibroblasts) and performed subcluster analysis (Fig. 2A) based on marker genes profiles published before[6,16,18,23-27] (Fig. 2B).Since dermal papilla (DP) cells ($Papp2^{+}Corin^{+}$) belongs to the existing HF in normal skin adjacent to the wound, which was not the focus of this part. We next conducted in-depth analysis of wound fibroblasts and defined them as following categories: upper layer papillary fibroblast (PF) ($Crabp1^{+}Fabp5^{+}$), lower layer fibroblast including reticular fibroblasts (RF) ($Dpp4^{+}Mgp^{+}Gpx3^{+}Plac8^{+}$) & hypodermis lipo-fibroblast (LF) ($Mfap4^{+}$ $Cd34^{+}$), as well as wound-activated myofibroblast ($Acta2^{+}Tagln^{+}Mki67^{+}$) and myeloid-derived adipocyte progenitors (Macf) ($Pdgfra^{+}$ $Lyz2^{+}$ $Ptprc^{+}$ $Plin2^{+}$). The composition of fibroblast subclusters from each group (Fig. 2C) might explain the reason why small wound generally heal with scarring devoid of HFs. In accordance with previous report[18], the major

initial wave of dermal repair in small wound is mediated by the lower lineage fibroblast including LF (49.88%) and RF (21.93%)(Fig. 2C), which is respectively related to hypodermis adipocytes formation and ECM collagen fibril organization (Fig. 2D).It has been proved that the inhibition of Dpp4 (marker gene of RF) activity could relieve the excessive fibrous scarring[28]. In contrast, there were more upper lineage PF (36.11%) in large wound (Fig. 2C). The PF in this dataset consisted of 2 subclusters including PF1(Runx1^{+}Inhba^{+})[23] and PF2(Notch1^{+}Prdm1^{+})[29], both of which were related to HF development (Fig. 2D). Intriguingly, there were 134 Macf cells specifically exist in large wound, which had been proved to be the progenitors of adipocyte around neo-HF in large wound center[24]. Next, we extracted cells assigned as keratinocyte and performed subcluster analysis. Known markers[8,16,26,30,31] were used to define keratinocyte subclusters identity (Fig. 2, E and G). HFSC (Lgr5^{+}Lrig1^{+})[8] and HFP (Msx2^{+}Krt28^{+}Mki67^{+})[31] were proved to be the dominant contributor to the de novo HF. The higher proportion of HFP in Ctrl_LW (12.97%) than Ctrl_SW (3.14%) may be another reason account for the initiation of WIHN specially in large wound. Besides, since the HF cycles through phases of growth (anagen), regression (catagen), and rest (telogen)[26]. Keratinocytes could be robustly assigned to two cell types: permanent part of the epidermis (interfollicular epidermis, sebaceous gland, and

non-cycling portion of the HF) and keratinocytes from the cycling part of the anagen HF. The anagen HF cells were composed of (Ube2c^{+}Ccnb1^{+}) germinative layer (GL) cells, (Mt4^{+} Rnaset2b^{+}Krt35^{+}) medulla (MED) and cortex cells, and (Krt25^{+}Krt27^{+}) inner root sheath (IRS) layers cells. Since the C57/B6 mice were in their second telogen (postnatal days P46–70) on POD7.The higher proportion of anagen HF cells in Ctrl_LW suggested a stronger HF telogen–anagen transition (TAT) around the large wound as well.

More abundant macrophages and more diverse heterogeneity of T cell from Ctrl_LW group

Next, we compared the immune cell heterogeneity between two groups. Macrophages are highly plastic immune cells upon different environment stimulators and contribute to most phases of tissue repair[32].They phagocytose pathogens or debris instantly in response to wounding. Then, they activate the adaptive immune system through specific antigen presentation, which is believed to bridge the innate and adaptive immune system[14].It has been reported that macrophage can selectively activate the specific wound-activated fibroblast subcluster [6] and play bidirectional role in skin fibrous scarring[7,33] or HF regeneration[8,34]. To explore the heterogeneity of macrophages, we extracted the monocyte and macrophages (MAC) and subjected them to further subcluster analysis. Canonical classification systems of macrophages including

“classically activated” M1 macrophages and “alternatively activated” M2 macrophages were shown insufficiently to identify the phenotypes in this condition (Fig. 3B).Based on known markers[16], three subsets including $Ccl8^{+}$ $Folr2^{+}C1qa^{+}Mrc1^{+}$ anti-inflammatory macrophages (AIM), $Ptgs2^{+}Ccl3^{+}Inhba^{+}Nos2^{+}$ pro-inflammatory macrophages (PIM) and $Ly6c2^{+}Plac8^{+}Cytip^{+}Clec4e^{+}$ monocyte (Mono) were determined (Fig. 3, A and C).It is noteworthy that Inhba (differentially expressed by PIM) was required for regenerative capacities in vertebrates[35]. The pseudo-temporal trajectory of the three subsets revealed that monocytes developed into PIM firstly and then polarized into AIM (Fig. 3E). KEGG enrichment analysis revealed that Mono might play role in antigen presentation and T cell differentiation, and Mono in Ctrl_LW group specifically related to nature killer cell mediated cytotoxicity; PIM was related to pro-inflammatory pathways, among which IL-17 pathway was up-regulated in Ctrl_LW group; AIM was correlated to lysosome, phagosome, and endocytosis which belonged to innate immune response (Fig. 3D).The higher proportion of all three macrophage subsets as well as neutrophil and dendritic cell in Ctrl_LW (Fig. S2) suggested there was a more complex environment both in innate immune response as well as the activation of adaptive system in large wound. The proportion of T cell was higher in Ctrl_LW group (Fig. S1B) in accordance with the result of Bulk-seq and histological results. Although the role of γδ T cells in

facilitating WIHN [9,11] has been demonstrated, the relationship of adaptive immune cells with HF regeneration is largely unknown till now. Based on published marker[16,36], T cells were clustered into seven subsets (Fig. 3, F and G) including Cd8b1^{+} cytotoxic T cell (CTL), Ifng^{+}Nkg7^{+}Xcl^{+} nature killer cell1 (NKT1), Ccl2^{+} nature killer cell2 (NKT2), Il17f^{+} T helper17 (Th17), Foxp3^{+} T regulatory cell (Treg), Trdv4^{+}Cd7^{+}Ctsw^{+} γδT cell1 (Tγδ1) and Cd7^{+}Ctsw^{+}Gnb21l^{+}γδT cell2 (Tγδ2). As shown in Fig. 3F, γδT cell was the major subtype of T cell in Ctrl_SW (70.82%), which was related to endocytosis in innate immune system (Fig 3H). In contrast, there were more abundant subtypes of adaptive αβT cells in Ctrl_LW group, which were related to Th17 and Th1/Th2 cell differentiation (Fig. 3H). Besides, NKT2 cell with highly expression of Ccl2 was also more in Ctrl_LW, which was related to the recruitment of inflammatory macrophage[37]. What's more, there were more Tregs in large wound which were believed to paly role in suppressing excessive collagen deposition and driving HFSC differentiation &migration[5]. To sum up, the diverse subtypes of T cell from Ctrl_LW group suggested a more complex adaptive immune micro-environment.

Identification of single-cell heterogeneity through the integration of spatial transcriptomics and sc-RNA seq profiling

To further explore the spatial characteristic of above cells in wound center or wound edge, we applied the spatial transcriptomics to analyze spatial gene expression profiles of small and large wound on POD7 (Fig. 4A). The epidermal, dermal, hypodermal layers and granulation tissue of the wounds were easily delineated histologically (Fig. 4B). Different regions from each group could be clearly distinguished on uniform manifold approximation and projection (UMAP) plot (Fig. 4C). Representative genes for each region were shown in Fig. S3A. We could find the clear outline of neo-epidermis based on Krt6a expression (as well as other keratinocyte related genes) (Fig. S3B). Similarly, fibroblast activity was evaluated using marker genes such as Col1a1, which were most dominant in granulation tissue (Fig. S3B). First, we extracted the epidermis and subjected it to the subcluster analysis (Fig. S4A). Based on published research[38,39], the repairing epidermis is organized into three regions: migration zone (migration-only), mixed zone (intermediate region of both proliferation and migration), and proliferation zone (proliferation-only region away from the wound) (Fig. S4, B and C).To overcome the low resolution of ST (one spot usually contains 1 to 10 cells), we integrated the ST and sc-RNA seq gene expression profiles using Addmodulescore function in Seurat[40].The top50 differentially expressed marker genes (ranked by avg_log2FC value) of each keretinocytes subclusters from sc-RNA seq (defined in Fig.2 E-F) were

used to score each ST spots gene expression profiles. The predicted spatial distributions for our scRNA-seq clusters were able to be projected to each spot using SpatialFeaturePlot function. As shown in the Fig. 4D, although Lgr5^{+} HFSC cells were less abundant in the neo-epithelium compared to Lgr6^{+} IFE basal cells. HFSC cells were shown to contribute to the developing migrating epidermis exclusively in large wound rather than small wound. Next, we extracted the granulation tissue and subjected it to the subcluster analysis. Unsupervised clustering categorized the granulation tissue into 13 clusters based on global gene expression patterns (Fig. S5 A-C). According to gene expression similarities, 13 unsupervised clusters were grouped into three functional clusters (FCs) including small wound (SW), upper layer of large wound (LW_upper) and lower layer of large wound (LW_lower) (Fig.S5D). GO analysis showed the LW_upper functional cluster (especially LW_Central1) was related to HF morphologies. Scoring spots in each section with fibroblast-signature genes from our scRNA-seq (defined in Fig.2 A-D) showed that the PF1 and PF2 (related to HF regeneration) exhibit strong spatial preferences within the large wound upper layer (especially wound center). In contrast, lower lineage fibroblasts including RF and LF preferentially resided in the large wound lower layer. In contrast, there was not any obvious aggregation tendency of fibroblast subpopulations in small wounds (Fig.4 E). It is noteworthy that lymphocyte chemotaxis and

antigen presentation related genes were enriched in migrating epidermis as well as upper layer of large wound. In contrast, there were innate immune system related genes that enriched in small wound (Fig.S4 D and S5 E). To explore how distinct immune cell types may contribute to the healing procedure in different wound size, the expression of known immune cell subclusters marker genes (defined in Fig.3) was surveyed. As shown in Fig.5 E, macrophages including AIM, PIM and Mono diffusely distributed in small wounds, while PIM (related to pro-inflammatory pathways) and Mono (related to antigen presentation) showed the preferentially aggregation in large wound center and wound margin. Besides, almost all T cell subclusters were exclusively expressed in large wound center and wound margin rather than small wound. To sum up, we observed the preferential aggregation of HFSC in migrating epithelium of large wound, and PF in upper layer (especially wound center) of large wound. These might be two aspects accounting for the exclusively presence of WIHN in large wound center. What's more, the spatial analysis of immune cell subclusters highlighted a special niche composed of PIM, Mono and T cells which co-localized with HFSC and PF (large wound margin and large wound center), which might in favor of tissue regeneration.

Cellular communication landscape between immune cell and HF-related cutaneous cell

To map potential interactions at different wound region, Cell Chat[41] was applied to compare the cell-cell communication patterns between sc-RNA seq datasets, and signaling pathways were next verified by visualizing the major ligands and receptors in ST sections (Fig. 5 A and B). By comparing the interaction strength (information flow), we could identify signaling pathways decrease (turn-off) or increase (turn-on) in different biologic conditions. As shown in Fig. S6, the bar graph showed significant signaling pathways ranked based on differences in the overall information flow. The top signaling pathways colored red were enriched in Ctrl_LW. Next, we selected those up-regulated pathways and compared the overall signaling strength of ligand-receptors that exhibit different signaling patterns (Fig. 5C). Consistent with the result of bulk-seq, adaptive immune system related pathways including MHC-I, MHC-II and CD80 was exclusively enriched in large wound. The major signaling among immune cell and keratinocyte/fibroblast in large wound was mediated by PF (related to HF regeneration). For example, as shown in Fig. 5 D, NKT2, γδ T, Th17 as well as PIM in large wound up-regulated the expression of IL-6. Correspondingly, the HFSC, PF1 and PF2 in large wound also expressed the Il6st (major receptor of IL-6 in IL6 signaling pathway). What’s more, PIM and Mono in large wound significantly up- regulated the expression of Inhba. Similarly, HFP, PF1 and PF2 in large wound also exclusively expressed the Acvr1b (major

receptor of Inhba in ACTIVIN signaling pathway). Spatial plots of Il6 and Inhba showed the preferentially aggregation of those ligands in large wound margin and center (co-localized with HFSC, PF as well as PIM, Mono, T cells). Collectively, our result illustrated that immune cells especially PIM, Mono and T cells may modulate the positioning and states of HFSC and PF through IL-6 and ACTIVIN signaling pathways. Together, these results uncovered the spatial heterogeneity of immune cell exclusively residing in large wound centern, and highlighted potential intercellular signaling pathways controlling the positioning and states of HF-associated HFSC and PF. The communication between immune and cutaneous cells was sophisticated, and these results might serve as a resource for further investigation of immune dynamics in scar-less skin regeneration.

More abundant neogenic HFs occurred in scaffold-implanted wounds with the further activation of adaptive immune system

Xenograft transplantation are one of the efficient treatments for severe large area wound of skin especially when patient's donor site is not qualified[42]. With the further understanding of tissue engineering, it is suggested that synthetic materials imitating the native structure of native ECM structure can integrate and play potentially pro-regeneration role to wound healing[13,43]. Our previous report has illustrated the pro-regenerative effect of aligned electrospinning scaffold with

approximate 300nm diameter fibrous in small wound [16,17] (diameter=0.6cm). Nevertheless, the influence of the polymer ECM scaffold over large wound healing and their impact on immune response still need further understood. We next repeated large full-thickness wound-healing experiments in C57BL/6 mice with/without implanted electrospinning membrane to investigate if the further regenerative phenomenon observed in ECM biosynthetic scaffold treated wounds. Workflow for evaluating large wound healing in C57BL/6 mice was summarized in Fig. 6A. We placed synthetic ECM scaffolds below the full-thickness excisional wound (diameter,1.5 cm; Fig. 6B) in ECM_LW group, while the Ctrl_LW group received no scaffolds. Wound coverage was faster in the ECM_LW group on POD7 (Fig. 6, C and E). The ECM_LW also had the smaller gap width on POD7 and POD14 (Fig. 6, D and F). On POD28, we found that ECM_LW group recapitulated normal skin architecture with equivalent number of dermal appendages and “basket-wave” ECM collagen deposition (Fig 6D). IF staining for Krt5 (keratin secreted by IFE basal cell) and Krt10 (keratin secreted by IFE differentiated cell) confirmed the ECM_LW group had the larger area of neo-epithelium (Fig. 6K). In summary, in mouse large full-thickness wound models, the aligned electrospinning membranes led to faster wound healing, reduced fibrotic response, and enhanced regeneration of HF compared to Ctrl group.

Bulk-RNA seq was performed for ECM_LW and Ctrl_LW samples harvested on POD7. Compared to the Ctrl_LW, the ECM_LW group showed increased enrichment of genes involved in the hair follicle development as well as T cell differentiation (Fig. 6H). KEGG analysis revealed elevated gene expression in leukocyte transendothelial migration signaling pathways for the ECM_LW group (Fig. 6H). Meanwhile, the volcano plot showed immunomodulatory properties related to the further activation of adaptive immune system in ECM_LW group (Fig. 6I). IF and IHC staining for Cd3 confirmed that increased adaptive T cell infiltration with implanted scaffold on POD 7 (Fig. 6J).

Sc-RNA revealed higher proportion of PF and HFP along with more T cell in scaffold-implanted large wound

Therefore, we sought to explore how ECM scaffold regulated the microenvironment in large wound. Hence, we used scRNA-seq to sequence cells from the wounded murine full-thickness skin on POD7 (Fig. S7A). We isolated cells from the ECM_LW and Ctrl_LW samples and applied them to the 10x scRNA-seq platform. After cell filtering, 31,740 single-cell transcriptomes were included in the final dataset (20,312 for the aligned group and 11,428 for the Ctrl group). Unsupervised clustering using Seurat categorized the cells into 10 main classes of cells (Fig. S7B). The composition of each cell cluster was listed so that the proportion of cells from two groups could be identified across

all cell clusters (Fig. S7B). Marker genes for each cell cluster were shown in the heatmap in (Fig. S7C). Genes related to T cells (Il7r, Areg and Tubb5) were substantially higher expressed by the ECM_LW (Fig. S7D). In mice, it has been shown that the implantation of xenogeneic dermal scaffolds does not induce a strong inflammatory response but has a strong impact on immune cell polarization, potentially inducing regenerative phenotypes[44]. We show that T cell differentiation in response to ECM scaffold implantation is driven toward regenerative subpopulations and found that acceleration of wound closure. Our study identified the therapeutic potential of T cells to initiate the regeneration of neotenic HFs and promote wound healing, providing a novel effective strategy to develop advanced cell therapies for severe large full-thickness wounds.

Discussion

- A new hair follicle has a growth cycle similar to normal hair follicles, but often without pigmentation. de novo follicles are separated from preexisting follicles by a hairless wound edge. New hair often appears in a zigzag shape with random growth orientation, different from normal hair, whose orientation is from head to tail, but often shares a common orientation within one cluster
- Macrophage: scar or WIHN
- T cell: γδT cell

Figure legends

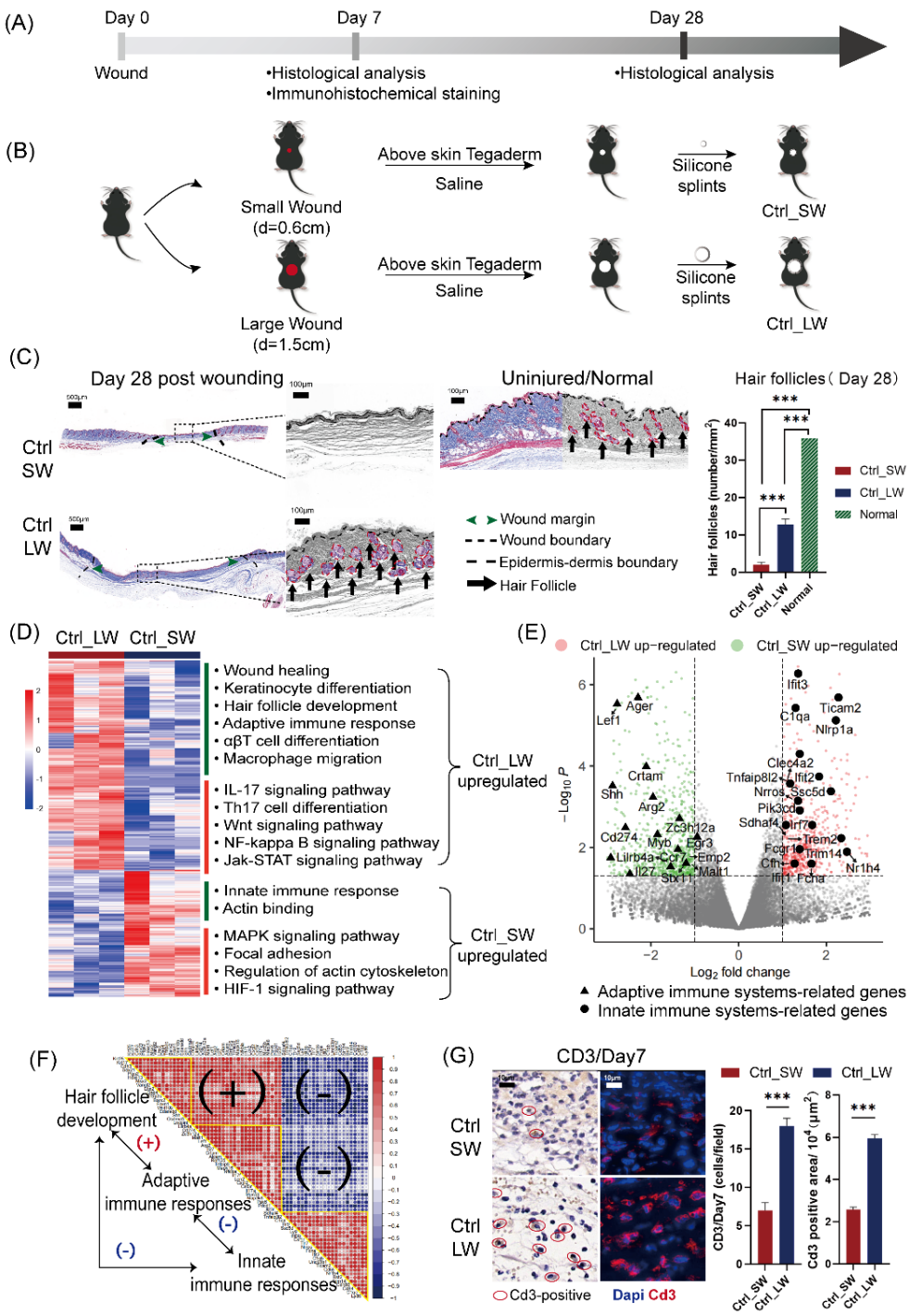

Fig.1. Evaluation of the healing of small or large full-thickness wound.

(A) Workflow for evaluating mice skin wound healing. (B) Surgical

process for the mice full-thickness excisional splinted wound. (C) H&E staining of normal skin or healed small (Ctrl_SW) and large (Ctrl_LW) full-thickness skin wound on POD 28, and histologic quantification of de novo hair follicles. (D) Heatmap showing hierarchical clustering of differentially expressed genes (p value<0.05 & |log2FC|> 1) and gene set enrichment analysis showing the up-regulated GO (green) and KEGG (red) pathways between two groups. (E) Volcano plot showing interested differentially expressed genes in two groups (Bulk RNA seq). (F) Immunofluorescence staining and Immunohistochemistry staining of Cd3 in wound center and corresponding quantification of $CD3^+$ cellular infiltration. (G) Pearson correlation analysis shows positive correlation between the expression of hair follicle development related genes, adaptive immune responses related genes and Innate immune responses related genes (positive, red; negative, blue).

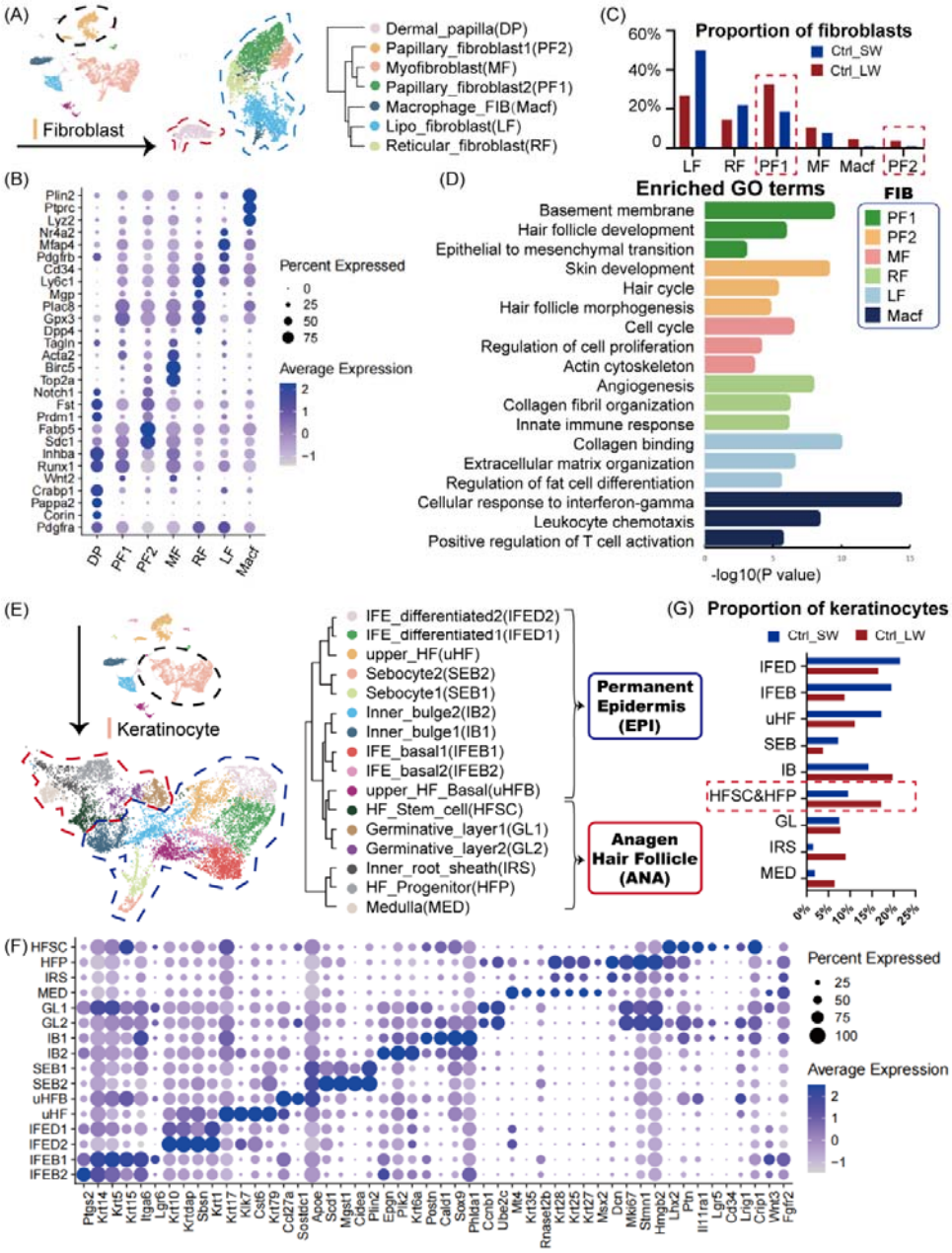

Fig.2. Further analysis of fibroblasts and keratinocytes between Ctrl_SW and Ctrl_LW. (A) Subclustering of fibroblasts showing 7 subsets; hierarchical clustering of average gene expression using pearson correlation analysis. (B) Marker genes for each fibroblasts subset. (C) Proportion of each subset in two groups. (D) GO enrichment analysis of

wound fibroblast subtypes. (E) Subclustering of keratinocytes showing 16 subsets; hierarchical clustering of average gene expression using pearson correlation analysis. (F) Marker genes for each keratinocytes subset. (G) Proportion of each keratinocytes subset in two groups.

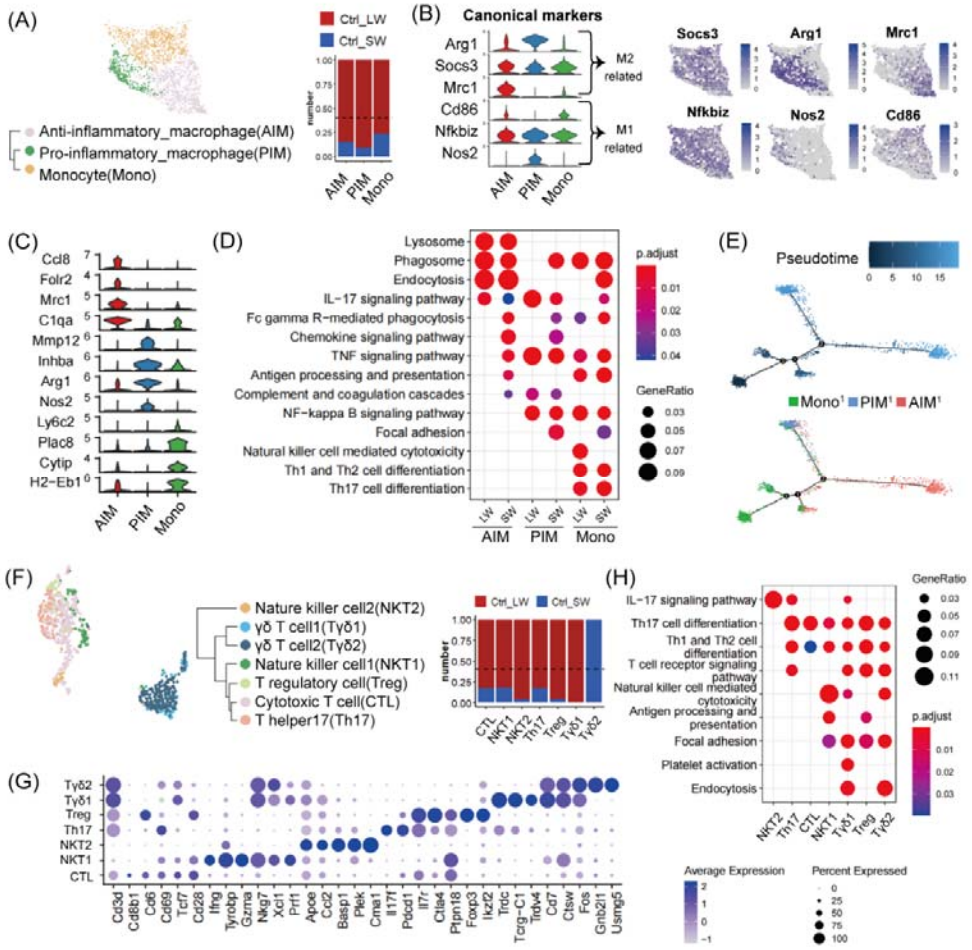

Fig.3. Analysis of Macrophages and T cells between Ctrl_SW and Ctrl_LW. (A) Subclustering of macrophages showing three subsets and hierarchical clustering of average gene expression (pearson correlation analysis); The composition for each subset was listed. (B) Expression of canonical M1 and M2 markers was inappropriate to identify the subtypes. (C) Marker genes for each macrophage/monocyte subset and (D) enriched gene sets in KEGG pathway analysis. (E) Pseudo-temporal ordering of macrophage/monocytes and the distribution of subsets. (F) Subclustering of T cells showing seven subsets and hierarchical

clustering of average gene expression (pearson correlation analysis); The composition for each subset is listed. (G) Marker genes for T cell subsets and (H) their enriched gene sets in KEGG analysis.

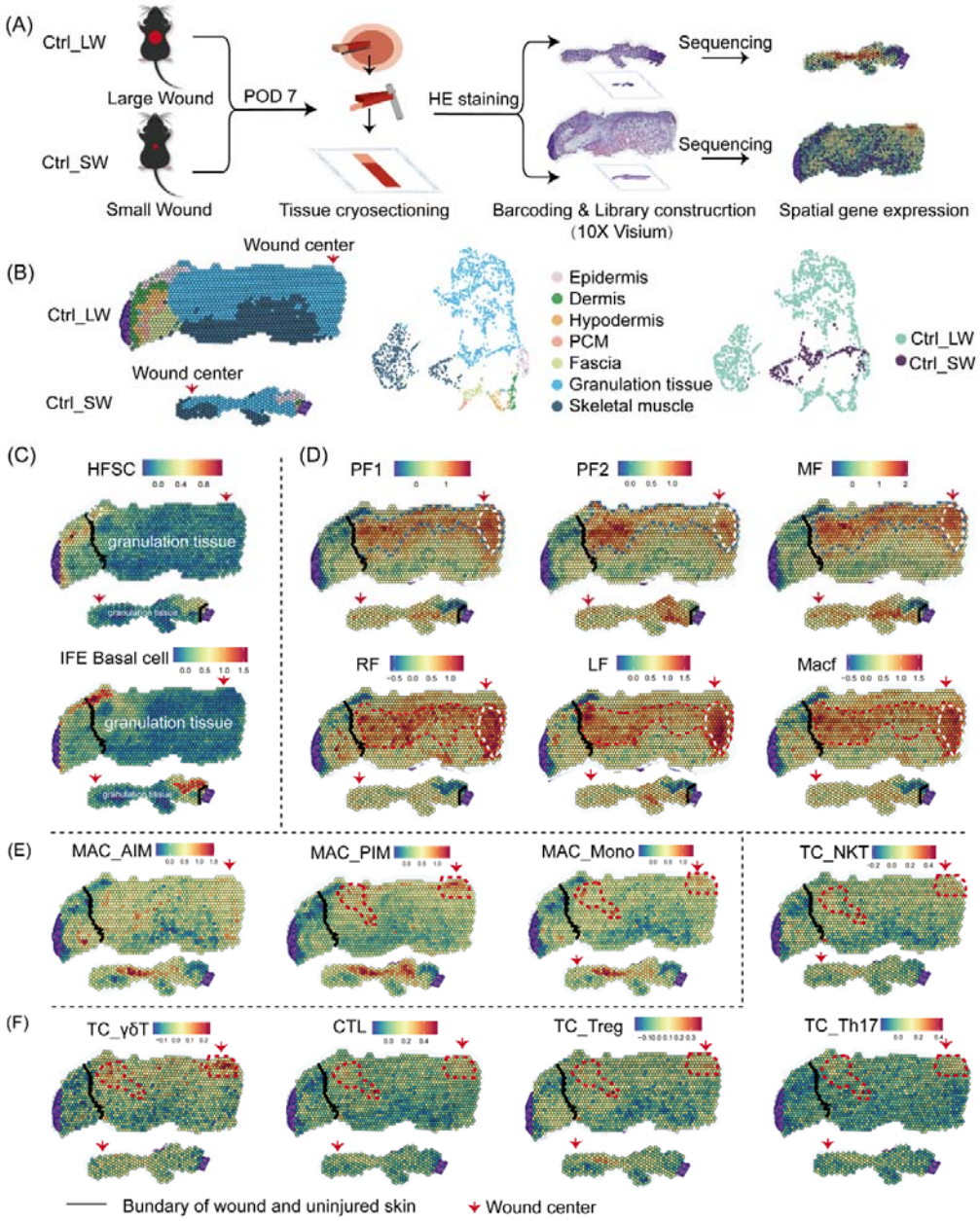

Fig. 4. Spatial transcriptomics applied to Ctrl_SW and Ctrl_LW. (A) Schematic for generating spatial transcriptomics data from splinted excisional wounds. Fresh wound tissue was harvested, flash frozen, embedded, and H&E staining. Each spot contained mRNA expression profiles of 1~10 cells. (B) Spatial plots and UMAP plot showing that the

seven regions could be distinguished by their transcriptional programs. Spatial feature plots showed defined keratinocyte (C), fibroblast (D), macrophage (E) and T cell (F) subclusters expression in tissue sections using Addmodulescore. Based on histological image, we could identify the wound center (red arrow) and separate the neo-epidermis migrating above the granulation tissue from unwound epidermis above the normal dermis away from the wound (black solid line).

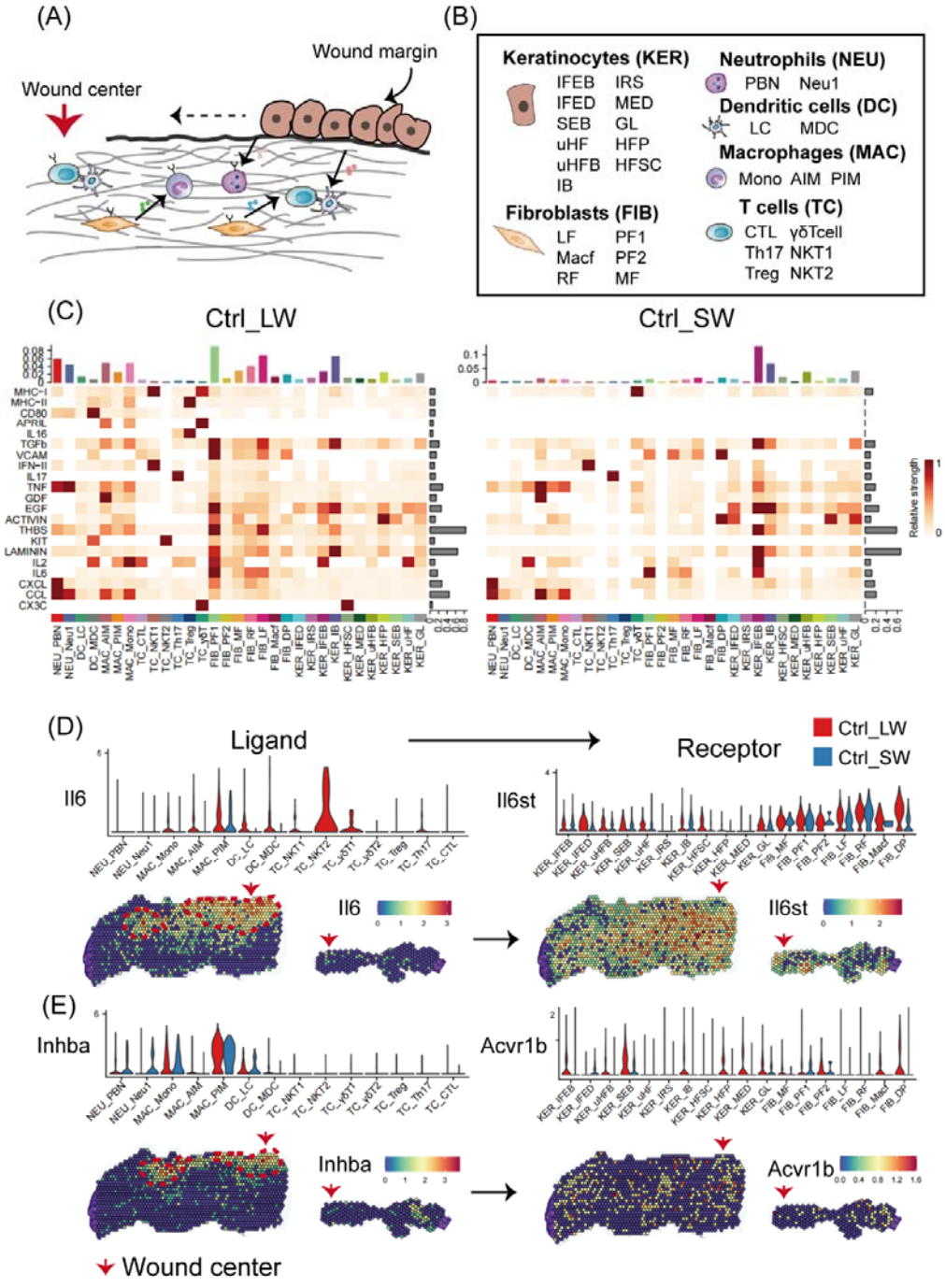

Fig. 5. Cellular communication landscape between immune cells and cutaneous cells in Ctrl_SW and Ctrl_LW. (A) Schematic of combined ligand-receptor analysis between keratinocytes, fibroblasts, and immune cells. (B) Defined subclusters in our sc-RNA seq dataset. (C) Comparison

of cell-cell communication patterns between Ctrl_SW and Ctrl_LW using CellChat. (D) Violin plot (sc-RNA) and spatial feature plots (ST) showed select ligands expressed by immune cell subpopulations and cognate receptor expression by keratinocytes and fibroblasts subtypes.

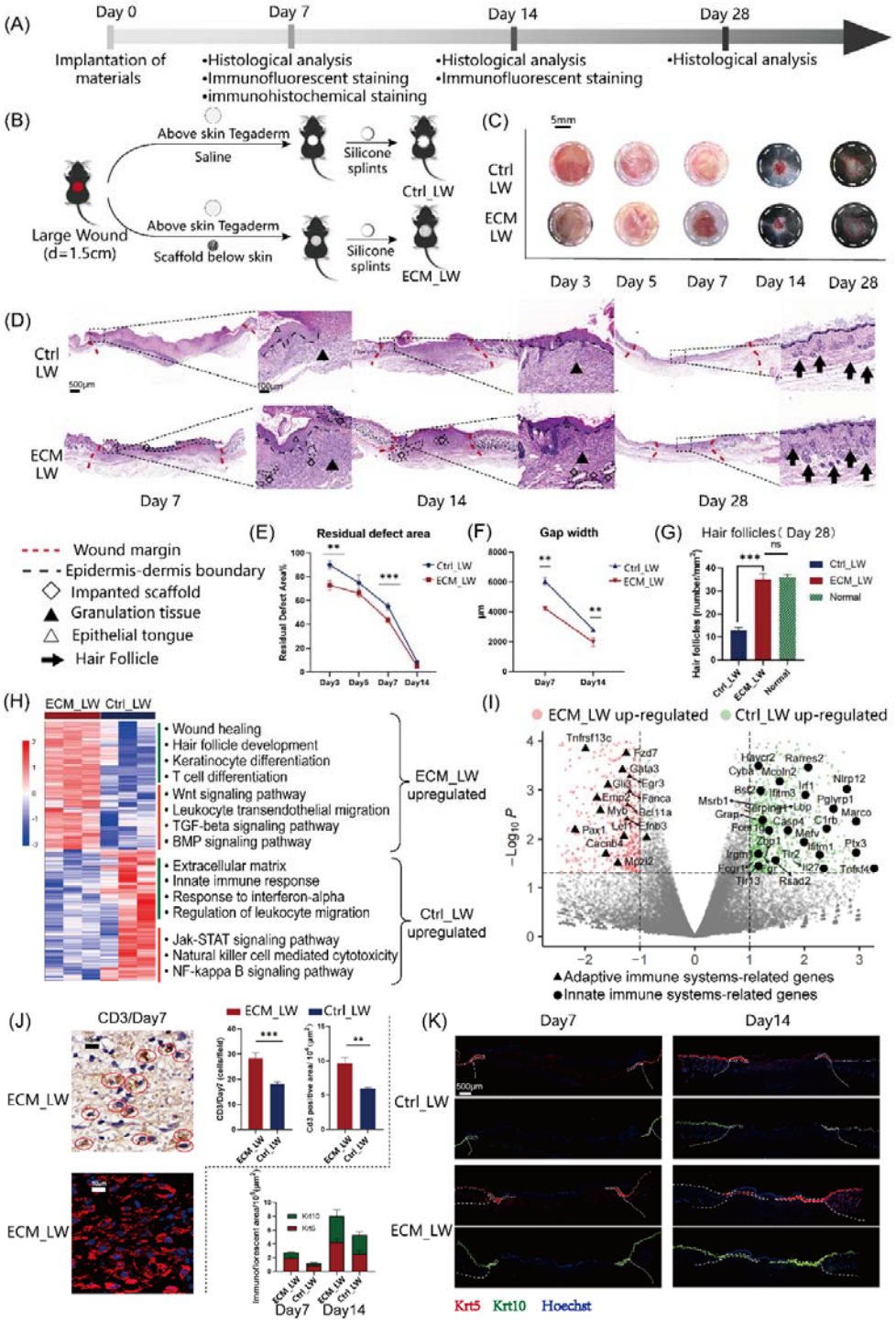

Fig 6 Evaluation of the healing of large full-thickness wounds with/without implanted ECM scaffolds. (A) Workflow for evaluating

mouse skin wound healing. (B) Surgical processes for mouse skin excisional wound model. (C and E) Residual wound area at 3, 5, 7, 14 and 28 days. (D) Histological analysis of Ctrl_LW and group implanted ECM scaffold. (F) Semiquantitative evaluation of gap width. (G) Histologic quantification of de novo hair follicles on POD28. (H) Heatmap showing hierarchical clustering of differentially expressed genes (p value<0.05 & |log2FC|> 1) and gene set enrichment analysis showing the up-regulated GO (green) and KEGG (red) pathways between two groups. (I) Volcano plot showing interested differentially expressed genes in two groups (Bulk RNA seq). (J) Immunofluorescence staining and Immunohistochemistry staining of Cd3 in wound center and corresponding quantification of $CD3^+$ cellular infiltration between Ctrl_LW and ECM_LW. (K) Immunofluorescent staining using Krt5 (red) and Krt10 (green) and semiquantitative evaluation of the fluorescent area.

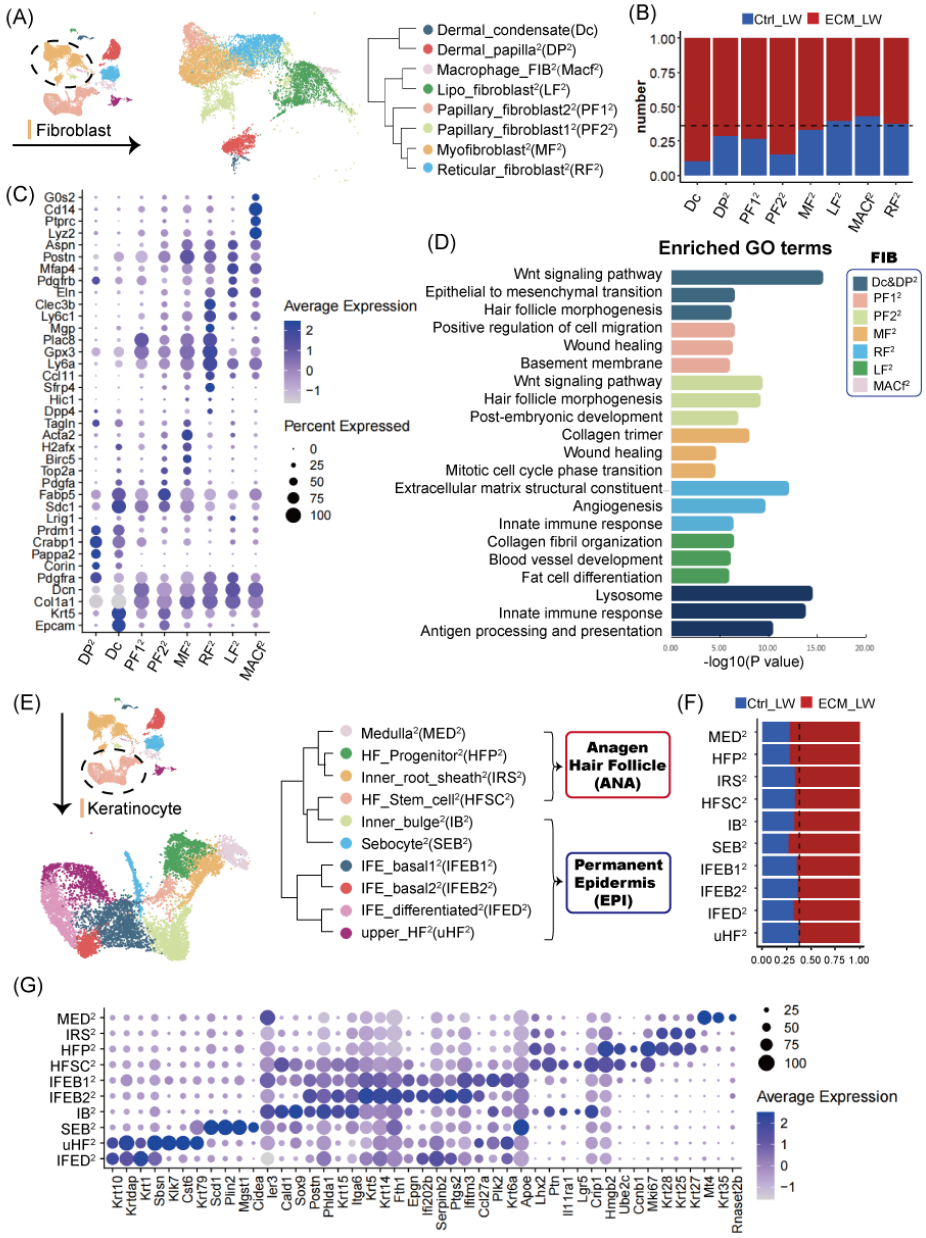

Fig 7 Further analysis of fibroblasts and keratinocytes between ECM_LW and Ctrl_LW. (A) Subclustering of fibroblasts showing 8 subsets; hierarchical clustering of average gene expression using pearson correlation analysis. (B) Proportion of each subset in two groups. (C) Marker genes for each fibroblasts subset. (D) GO enrichment analysis of

wound fibroblast subtypes. (E) Subclustering of keratinocytes showing 10 subsets; hierarchical clustering of average gene expression using pearson correlation analysis. (F) Proportion of each keratinocytes subset in two groups. (G) Marker genes for each keratinocytes subset.

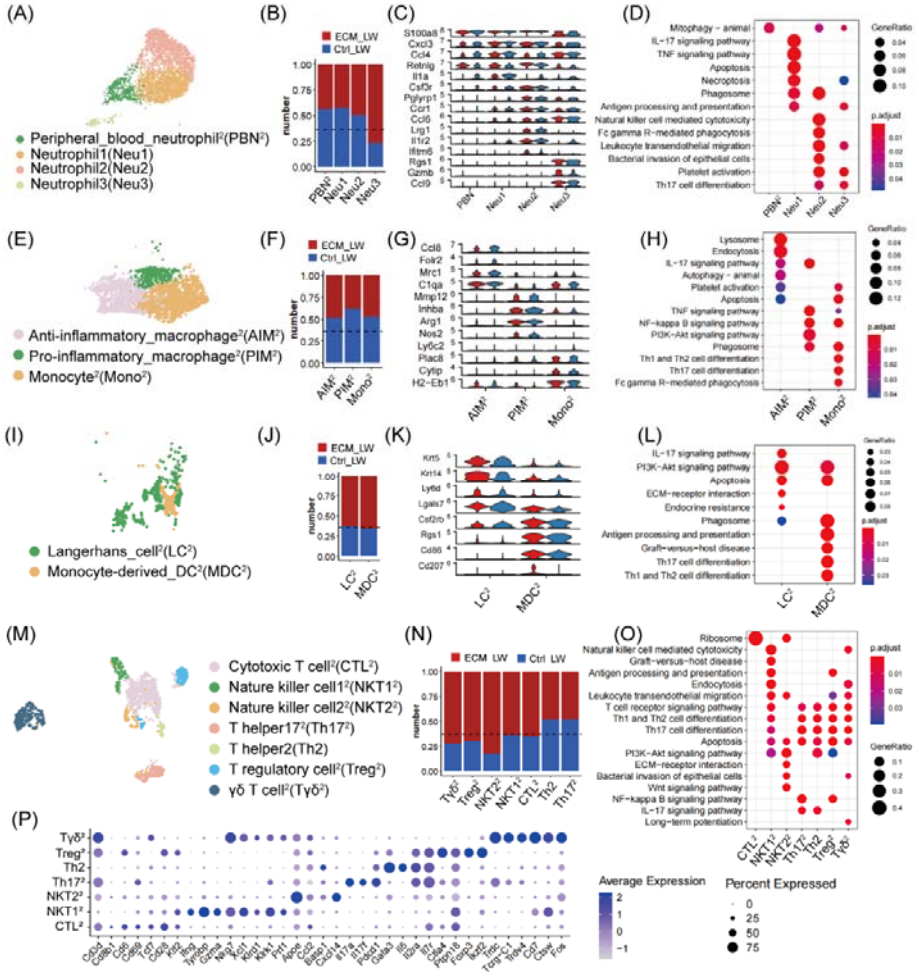

Fig 8. Analysis of immune cells between ECM_LW and Ctrl_LW. (A) Subclustering of neutrophils showing four subsets; (B) The composition for each subset is listed. (B) Expression of canonical M1 and M2 markers was inappropriate to identify the subtypes. (C) Marker genes for each macrophage/monocyte subset and (D) enriched gene sets in KEGG pathway analysis. (E) Pseudo-temporal ordering of macrophage/monocytes and the distribution of subsets. (F) Subclustering of T cells showing seven subsets and hierarchical clustering of average

gene expression (pearson correlation analysis); The composition for each subset is listed. (G) Marker genes for T cell subsets and their enriched gene sets in KEGG analysis (A) Subclustering of macrophages showing three subsets and hierarchical clustering of average gene expression (pearson correlation analysis); The composition for each subset is listed. (B) Expression of canonical M1 and M2 markers was inappropriate to identify the subtypes. (C) Marker genes for each macrophage/monocyte subset and (D) enriched gene sets in KEGG pathway analysis. (E) Pseudo-temporal ordering of macrophage/monocytes and the distribution of subsets. (F) Subclustering of T cells showing seven subsets and hierarchical clustering of average gene expression (pearson correlation analysis); The composition for each subset is listed. (G) Marker genes for T cell subsets and their enriched gene sets in KEGG analysis (H).

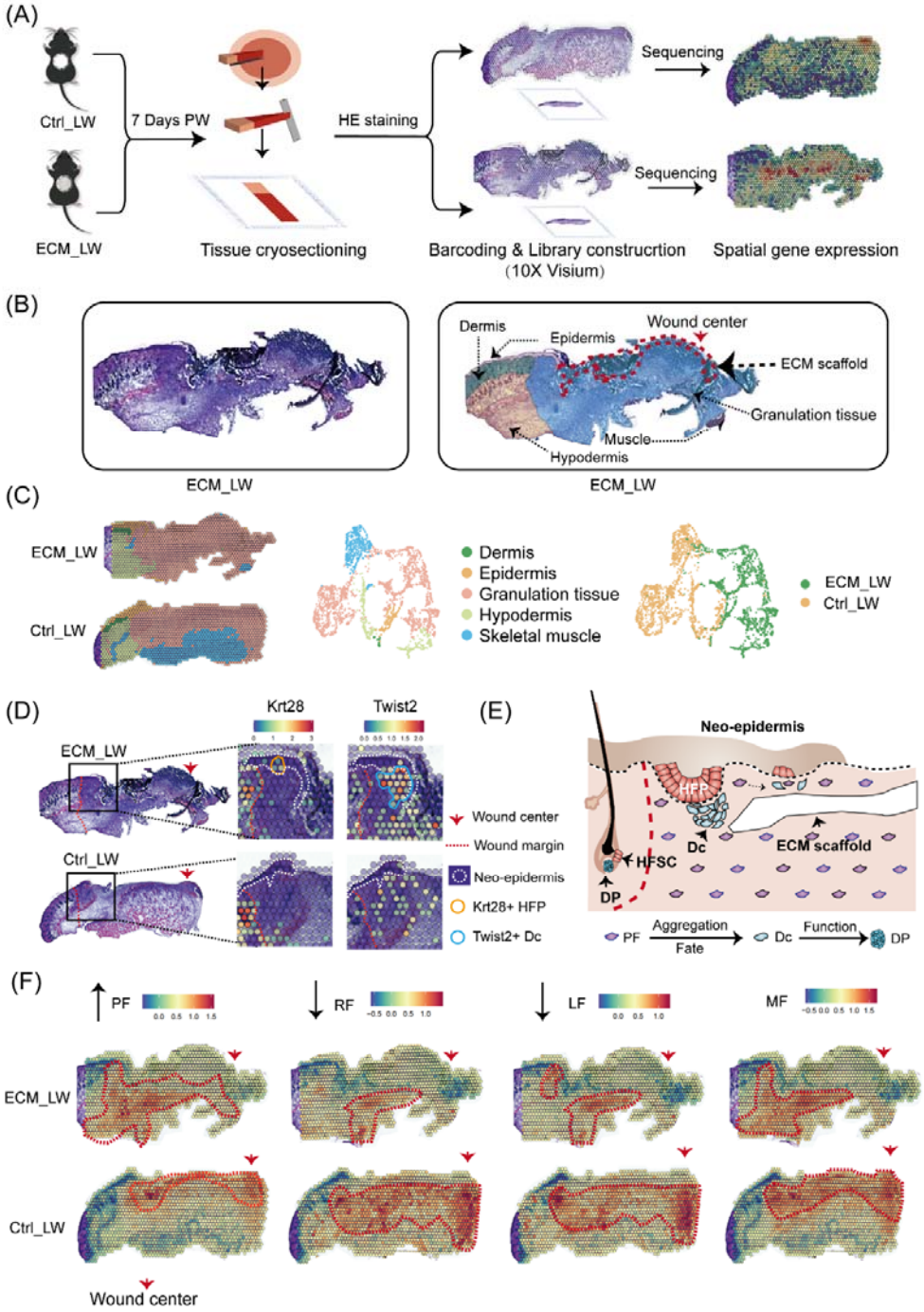

Fig.9. Spatial transcriptomics applied to ECM_LW and Ctrl_LW. (A) Schematic for generating spatial transcriptomics data from splinted excisional wounds. Fresh wound tissue was harvested, flash frozen,

embedded, and H&E staining. Each spot contained mRNA expression profiles of 1~10 cells. (C) Spatial plots and UMAP plot showing that the five regions could be distinguished by their transcriptional programs. (D) Spatial feature plot showed the expression of Krt28 and Twist2 in migrating neo-epidermis. (E) Illustration showed the wound healing with de novo HF formation. (F) Spatial feature plots showed defined fibroblast subclusters expression in tissue sections using Addmodulescore.

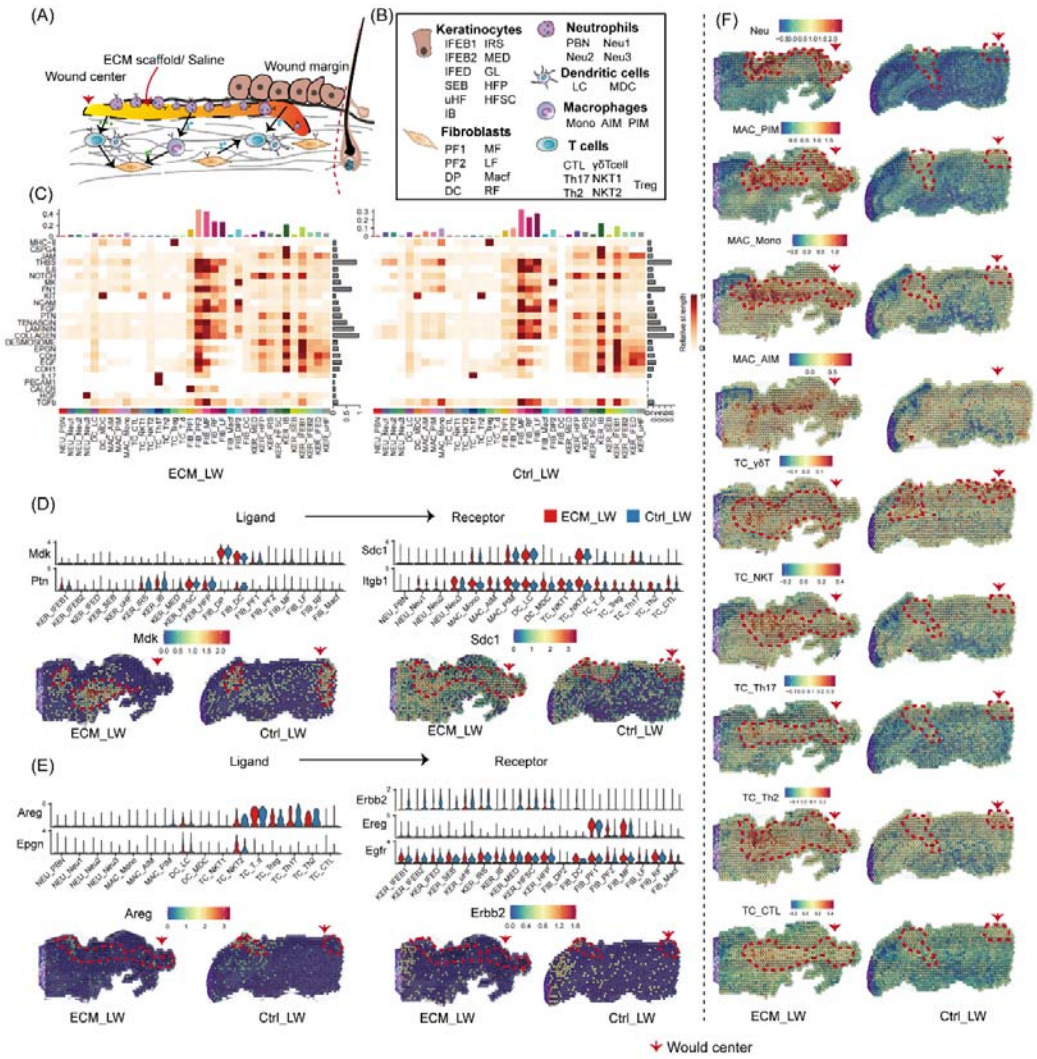

Fig.10. Cellular communication landscape between immune cells and cutaneous cells in ECM_LW and Ctrl_LW. (A) Schematic of combined ligand-receptor analysis between keratinocytes, fibroblasts, and immune cells. (B) Defined subclusters in our sc-RNA seq dataset. (C) Comparison of cell-cell communication patterns between ECM_LW and Ctrl_LW using CellChat. (D) Violin plot (sc-RNA) and spatial feature plots (ST) showed select ligands expression (immune cells) and cognate receptor expression (cutaneous cells). (E) Violin plot (sc-RNA) and

spatial feature plots (ST) showed select ligands expression (cutaneous cells) and cognate receptor expression (immune cells). (F) Spatial feature plots showed defined macrophages and T cells subclusters expression in tissue sections using Addmodulescore.

Materials and methods

Fabrication of biosynthetic ECM scaffolds

The preparation of biosynthetic ECM membranes was similar to our previous report[17].To fabricate the electrospinning scaffold with approximate 300nm diameter aligned fibers, 20% w/v PLGA (LA/GA = 75:25, molecular weight = 105 kDa, Jinan Daigang Biomaterial Co. Ltd.) and 2% w/v FC (Sangon Biotech Co. Ltd.) were dissolved in HFIP (Aladdin Co., Ltd.) with stirring until complete dissolution. The solution was fed at 0.018mm/min, and a voltage of -2/5kv and 11 cm distance between the needle (21G) and the rotating cylinder (2800 rpm) was applied. After been dried in a vacuum oven for a week, The morphology of PLGA/FC nanofibrous scaffold was observed by the scanning electron microscopy (SEM; JSM-7500F, JEOL, Japan). The scaffolds were cut into circular shape (0.8cm or 1.8cm in diameter) and sterilized using γ-irradiation before the animal implantation experiments.

Excisional wound model and implantation procedures

All procedures involving animals were approved by the Institution Review Board of West China Hospital of Stomatology (No. WCHSIRB-D-2017-033-R1). Female and male C57BL/6J mice (Dossy Experimental Animals Co., Ltd.), at the age of 6 week (~20 g) were used in this research. The large (1.5cm in diameter) and small (0.6cm in diameter) full-thickness skin wound were created in the mice dorsal skin.

The mice in this study were divided into four groups: small wounds transplanted with saline (Ctrl_SW) or biosynthetic ECM scaffolds below the wound (ECM_SW), and large wound transplanted with saline (Ctrl_LW) or biosynthetic ECM scaffolds below the wound (ECM_LW). Subsequently, the wounds were covered with sterile Tegaderm film (3M) and respectively fixed on the small (inner diameter 8 mm and outer diameter 12 mm, for small wound) or large (inner diameter 18 mm and outer diameter 22 mm, for large wound) silicone ring with uniform suture. Mice were euthanatized at 1, 2, and 4 weeks after the surgery, and the small (diameter 10 mm, for small wound) or large (diameter 25 mm, for large wound) round full-thickness sample was harvested.

Bulk RNA sequencing

Three replicates of mice skin wounds in each group were collected for the of Bulk RNA sequencing procedure. Total amounts and integrity of RNA were assessed using the RNA Nano 6000 Assay Kit of the Bioanalyzer 2100 system (Agilent Technologies, CA, USA). mRNA was purified from total RNA by using poly-T oligo-attached magnetic beads. The library fragments were purified with AMPure XP system (Beckman Coulter, Beverly, USA). The PCR amplification product was purified by AMPure XP beads. After the library is qualified by qRT-PCR, the different libraries are pooling and being sequenced by the Illumina NovaSeq 6000. FeatureCounts (v1.5.0-p3) was used to count the reads numbers mapped

to each gene. And then FPKM of each gene was calculated based on the length of the gene and reads count mapped to this gene. Differential expression analysis of two groups (three biological replicates per group) was performed using the DESeq2 R package (1.20.0), p−value <0.05 and $|\log_2(\text{foldchange})|$ >1 were set as the threshold for significantly differential expression. GO terms and KEGG pathways with corrected P-value less than 0.05 were considered significantly enriched by differential expressed genes.

Single cell RNA sequencing

Specimen harvest procedure for scRNA-seq was like our previous report[16],3~4 fresh samples were collected per group. In brief, the wound tissues were firstly digested by the Epidermis Dissociation Kit (Epidermis Dissociation Kit, mouse; Miltenyi Biotec) for enzymatic epidermal-dermal separation. The epidermis part was dissociated by a gentleMACS Dissociator (Miltenyi), then filtered (70-mm cell strainer, Corning, Durham), centrifuged (300g, 10 min, 4°C), and resuspended with phosphate-buffered saline (PBS) containing 0.5% bovine serum albumin (BSA). The dermis part was cut into 1 mm width pieces and mixed with mixed enzyme solution containing type I collagenase (Gibco, Grand Island) and trypsin (Gibco, Canada), then dissociated by gentleMACS Dissociator (Miltenyi), and digested for 2.5 hours in a hybridization oven (Peqlab PerfectBlot). After being dissociated, filtered,

centrifuged, and resuspended in red blood cell lysis buffer (Solarbio), the dermis cells were mixed with epidermis part. Then the dead cells and debris were removed by Dead Cell Removal MicroBeads (Miltenyi). Lastly, these suspensions were then carried out for Single-Cell RNA-seq (10x Genomics Chromium Single Cell Kit). Sequencing (10x Genomics Chromium Single Cell 3′ v3) was performed using an Illumina 1.9 mode. Then, reads were aligned, and expression matrices were generated for downstream analysis (Cell Ranger pipeline software). Filtering, normalization, scaling and canonical correlation analysis were performed (Seurat 4.1.2.) for integrated datasets. CellChat was used to predict receptor-ligand probability among cell subpopulations.

Spatial Transcriptomics

Fresh samples were rapidly harvested and frozen in OCT. Wound tissues were cryosectioned at -20 degrees onto gene expression slides. Tissue sections on the Capture Areas of the Visium Spatial Gene Expression are fixed using methanol, H&E staining images will be used downstream to map the gene expression patterns. Using the Visium Tissue Optimization Slide & Reagent kit, permeabilization time was optimized. Second Strand Mix is added to the tissue sections to initiate second strand synthesis. After transfer of cDNA from the slide, spatially barcoded, full-length cDNA is amplified via PCR to generate sufficient mass for library construction. The final libraries contain the P5 and P7 primers used in

Illumina amplification. A Visium Spatial Gene Expression library comprises standard Illumina paired-end constructs which begin and end with P5 and P7. Raw FASTQ files and histology images were processed (SpaceRanger software) for genome alignment. Raw output files for each group were read into R studio(Seurat 4.1.2). Normalization across spots was performed with the SCTransform function. The spatial cluster gene signature overlap correlation matrix was generated by first taking all genes differentially expressed (average logFC > 0.2 and adjusted p value < 0.05 across all ST clusters. Pearson correlation was calculated across this matrix and hierarchical clustering of ST clusters was performed with the heatmap function with the ggplots package. Signature scoring derived from scRNA-seq and ST signatures was performed with the AddModuleScore function.

Histopathology, Immunohistochemistry, and immunofluorescence microscopy

The samples were fixed with 4% paraformaldehyde at least 48 hours before ethanol and xylene dehydration. H&E staining and Masson's trichrome staining were performed for the observation of re-epithelialization and collagen fiber deposition. Immunofluorescence staining for cytokeratin 5 (ab52635, Abcam, 1:200) and cytokeratin 10 (ab76318, Abcam, 1:150) and was performed for to assess keratinization. Immunofluorescence and immunofluorescence staining for Cd3 (ab52635,

Abcam, 1:200) and Cd68(ab76318, Abcam, 1:150) was performed for the quantification the infiltration of T cells and macrophages.

Statistics and reproducibility

At least three independent replicates were conducted to obtain repeatable data, and the data was dealt with Case Viewer software, Image J software, and Prism 8.0 software. Statistical analyses were performed by Student's t-test or one-way analysis of variance (ANOVA) with Tukey post-hoc test. The numerical data are presented as mean ± standard deviation. A value of $p < 0.05$ was considered statistically significant (*$p < 0.05$, **$p < 0.01$, ***$p < 0.001$), and ns means no statistically significant difference.

CRediT authorship contribution statement

Yang Yang: Formal analysis, Investigation, Validation, Writing original draft, Resources. **Chenyu Chu:** Project administration, Methodology, Writing – review & editing. **Chen Hu**: Data curation. **Chenbing Wang:** Software, Data curation. **Shengan Rung:** Formal analysis, Data curation, Investigation. **Yili Qu:** Funding acquisition, Supervision. **Yi Man**: Project administration, Funding acquisition.

Declaration of competing interest

The authors state no conflict of interest.

Acknowledgments

This work was supported by Key R & D Projects of Sichuan Science and Technology Plan (2022YFS0041), Interdisciplinary Innovation Project,

West China Hospital of Stomatology Sichuan University (RD-03-202006), and Research and Develop Program, West China Hospital of Stomatology Sichuan University (No. LCYJ2019-19). We would like to thank the Novogene company for RNA sequencing work, thank the National Clinical Research Center for Oral Diseases & State Key Laboratory of Oral Diseases for sample harvest and Histological analysis, and thank the Analytical & Testing Center of Sichuan University for the fabrication of biosynthetic ECM scaffolds.

Abbreviations:

ECM: Extracellular matrix

PLGA: Poly (lactide-co-glycolide)

FC: Fish collagen

HFIP: 1,1,1,3,3,3- Hexafluoro-2-propanol

NHS: N-hydroxysuccinimide

EDC: 1- ethyl-3-(3-dimehylaminopropyl) carbodiimide hydrochloride

SEM: Scanning electron microscopy

MST: Masson's trichrome

IHC: Immunohistochemistry

ANOVA: Analysis of variance

GO: Gene Ontology

KEGG: Kyoto Encyclopedia of Genes and Genomes

PBS: Phosphate-buffered saline

BSA: Bovine serum albumin

POD: Postoperative days

scRNA-seq: Single-cell RNA sequencing

bulk-seq: Bulk-tissue RNA sequencing

ST: spatial transcriptomics

TAT: telogen–anagen transition

DC: dendritic cells

Reference

Supplementary files:

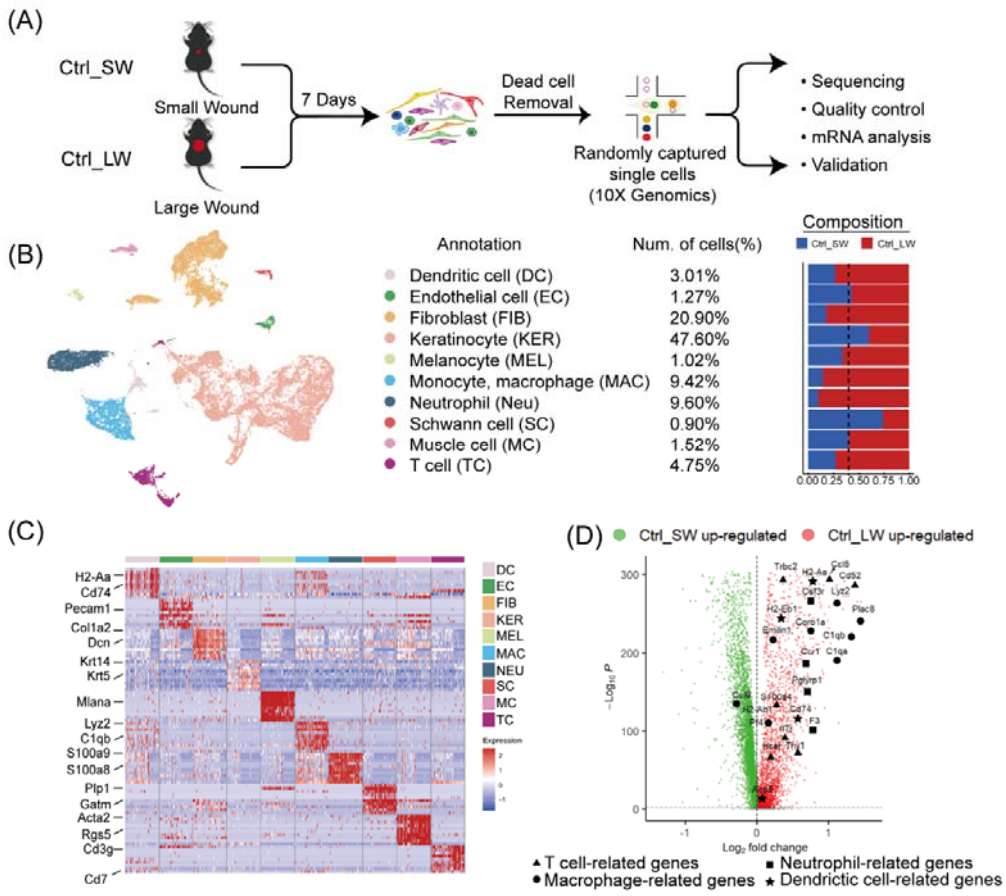

Fig.S1. Overview of the single-cell transcriptome analysis between Ctrl_SW and Ctrl_LW. (A) Single-cell experiment workflow. (B) Cells were categorized into 10 main clusters. The number of cell populations in each cluster, number of cells (%), and composition of Ctrl_SW and Ctrl_LW groups were listed. (C) Heatmap and top10 marker genes for different clusters. (D) Volcano plot showing interested differentially expressed genes in Ctrl_SW and Ctrl_LW group (Sc-RNA).

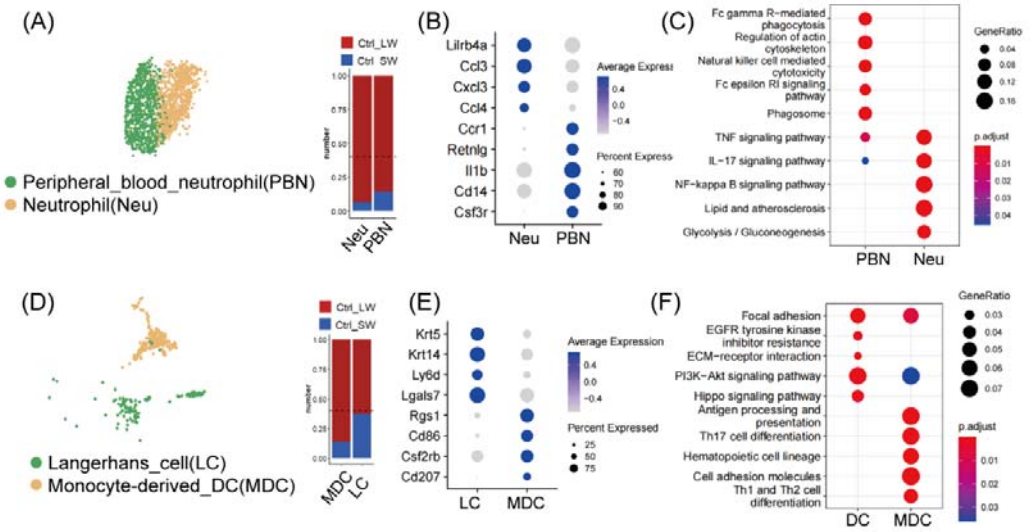

Fig.S2. Further sc-RNA seq analysis of neutrophils and dendritic cells between Ctrl_SW and Ctrl_LW. (A) Subclustering of neutrophils showing 2 subsets. The composition for each subset is listed. (B) Marker genes for each neutrophil subset. (C) Gene enrichment analysis of KEGG pathway. (D) Subclustering of dendritic cells showing two subsets. The composition for each subset is listed. (E) Marker genes for each dendritic cells subset. (F) Gene enrichment analysis of KEGG pathway.

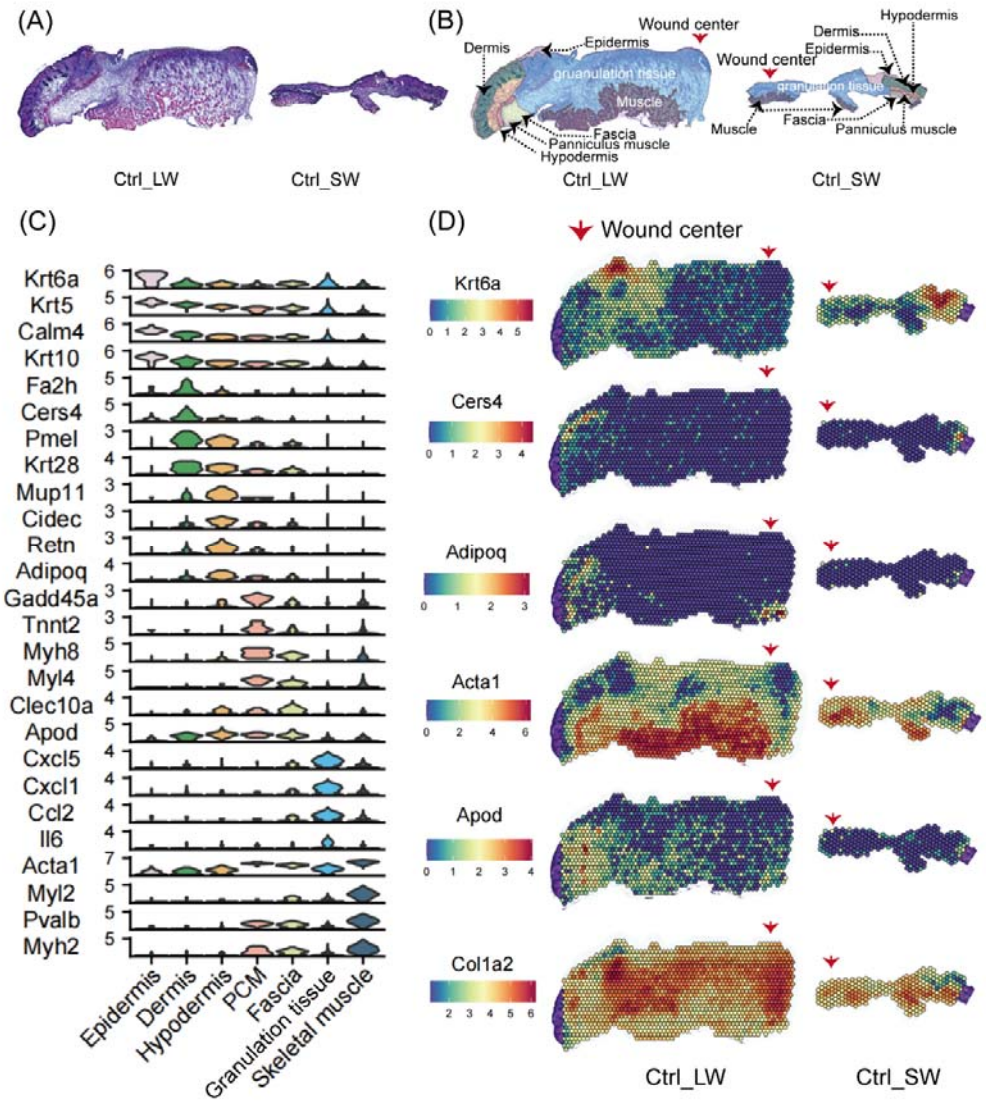

Fig.S3. Spatial transcriptomics profiles of Ctrl_SW and Ctrl_LW. (A) Original histological images. (B) The annotations indicated the anatomical structures. (C) Stacked violin plot shows marker genes differentially expressed in each region. (D) Spatial Feature Plot showed representative marker gene of each region.

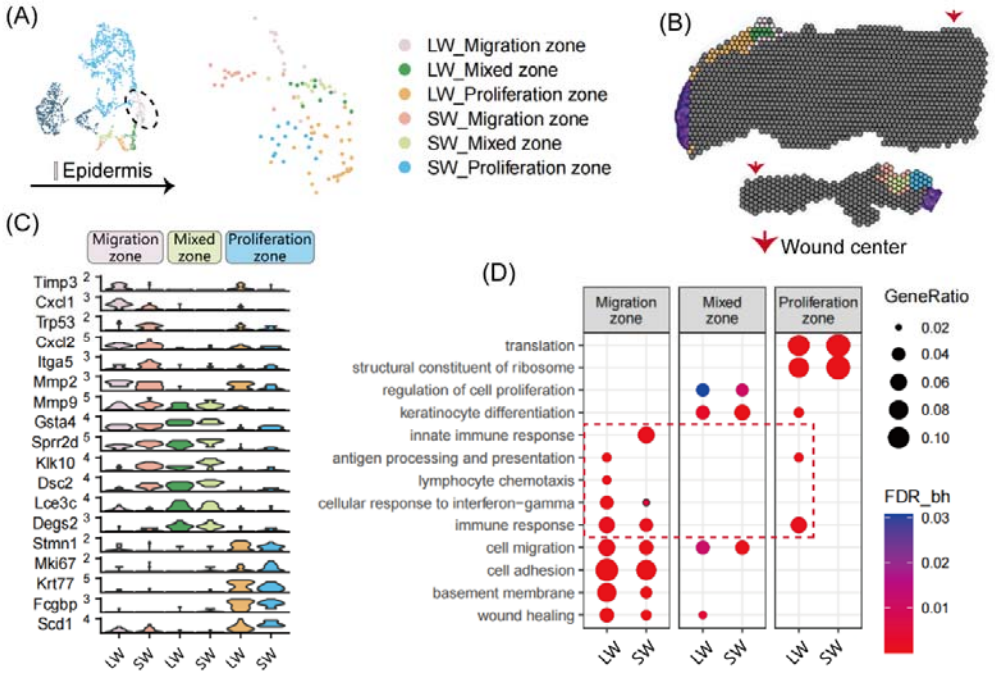

Fig.S4. Further subclustering analysis of epidermis in Ctrl_SW and Ctrl_LW. (A)Subsets of epidermis in each group. (B) Corresponding spatialplot of subclusters. (C) StackedVlnPlot shows marker genes differentially expressed in each cluster. (D) KEGG enrichment analysis of each subclusters

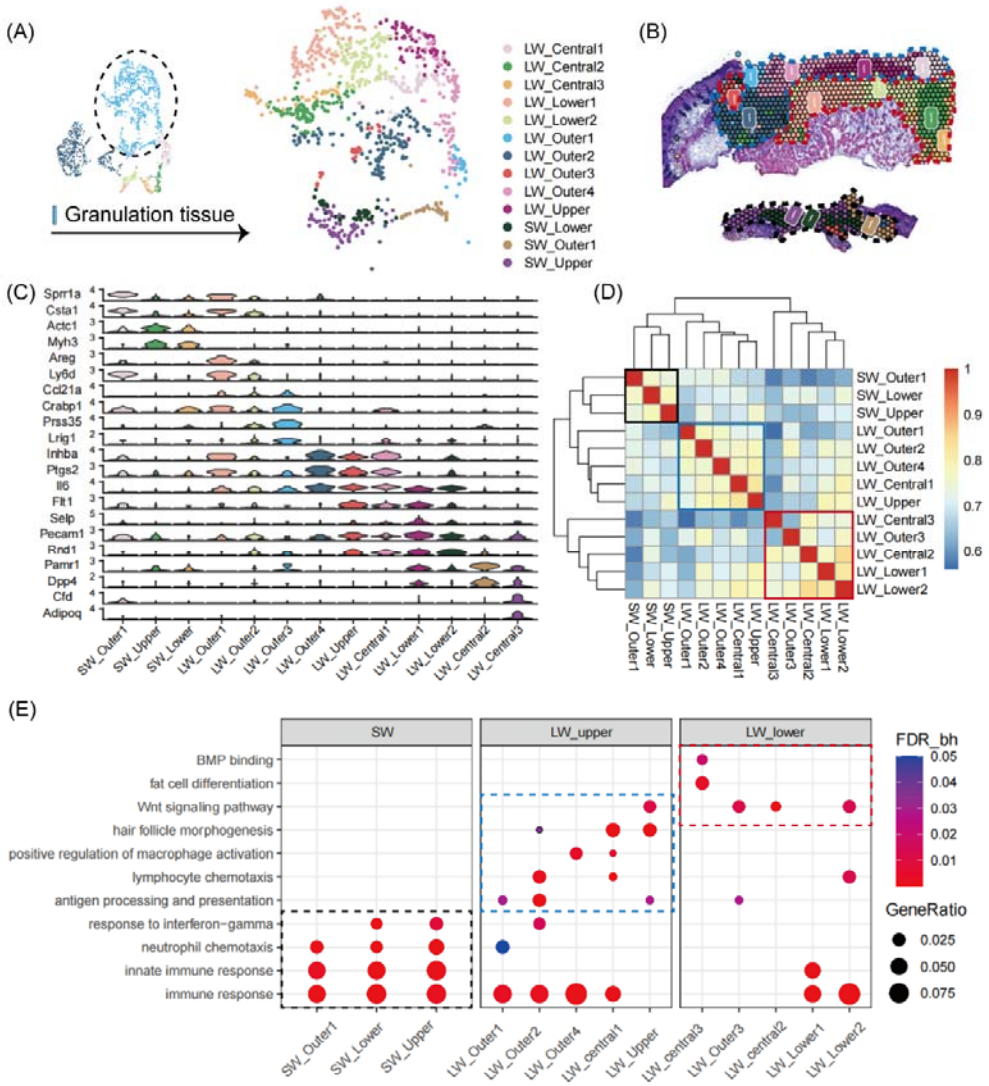

Fig.S5. Further subclustering analysis of granulation tissue in Ctrl_SW and Ctrl_LW. (A)Subsets of granulation tissue in each group. (B) Corresponding spatialplot of subclusters. (C) StackedVlnPlot shows marker genes differentially expressed in each cluster. (D) 13 regions were grouped into three functional clusters (FCs) by Pearson correlation analysis. (E) KEGG enrichment analysis of each subclusters.

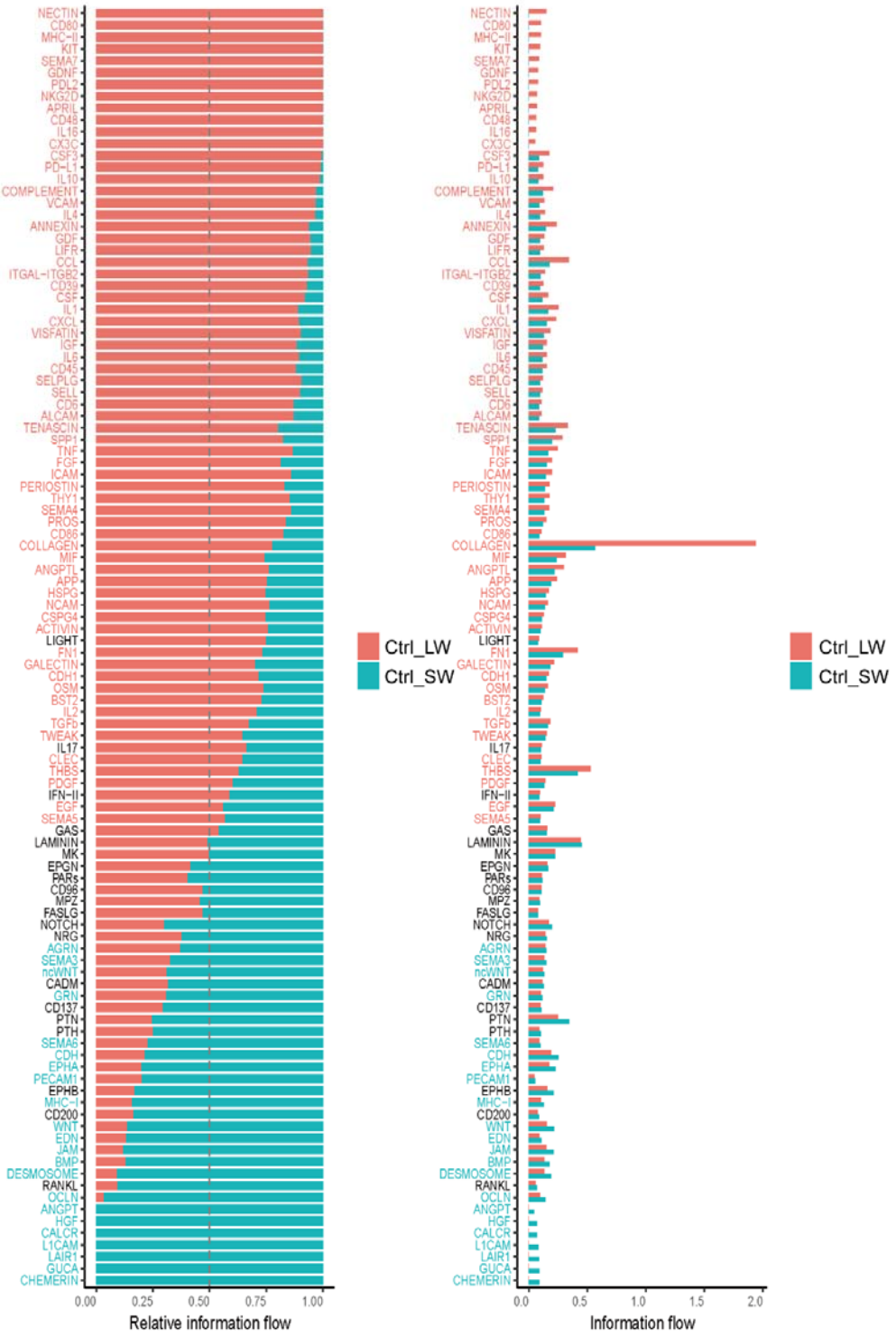

Fig.S6. Comparison of the overall information flow between Ctrl_SW and Ctrl_LW. Bar graph showed significant signaling pathways which

were ranked based on differences in the overall information flow between Ctrl_SW and Ctrl_LW. The top signaling pathways colored red are enriched in Ctrl_LW, and these colored green were enriched in the Ctrl_SW.

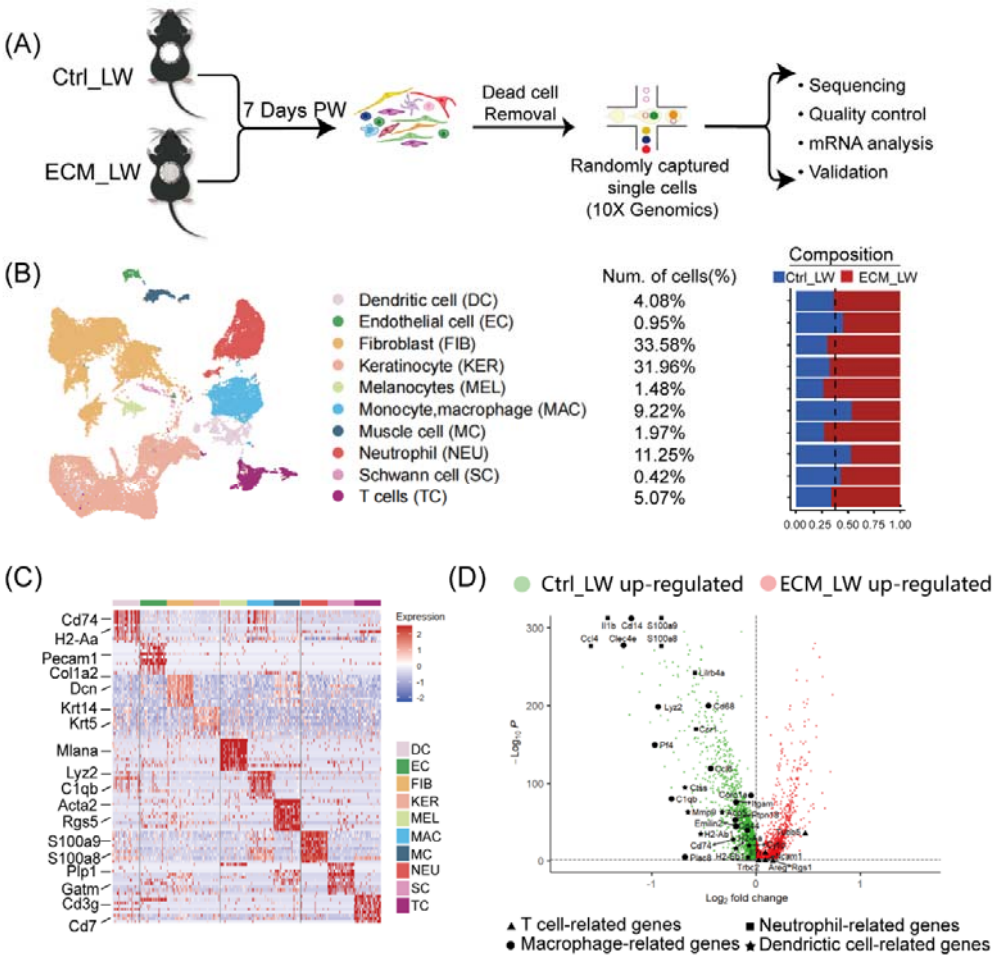

Fig.S7. Overview of the single-cell transcriptome analysis between ECM_LW and Ctrl_LW. (A) Single-cell experiment workflow. (B) Cells were categorized into 10 main clusters. The number of cell populations in each cluster, number of cells (%), and composition of ECM_LW and Ctrl_LW groups were listed. (C) Heatmap and top10 marker genes for different clusters. (D) Volcano plot showing interested differentially expressed genes in Ctrl_LW and Ctrl_LW group (sc-RNA).

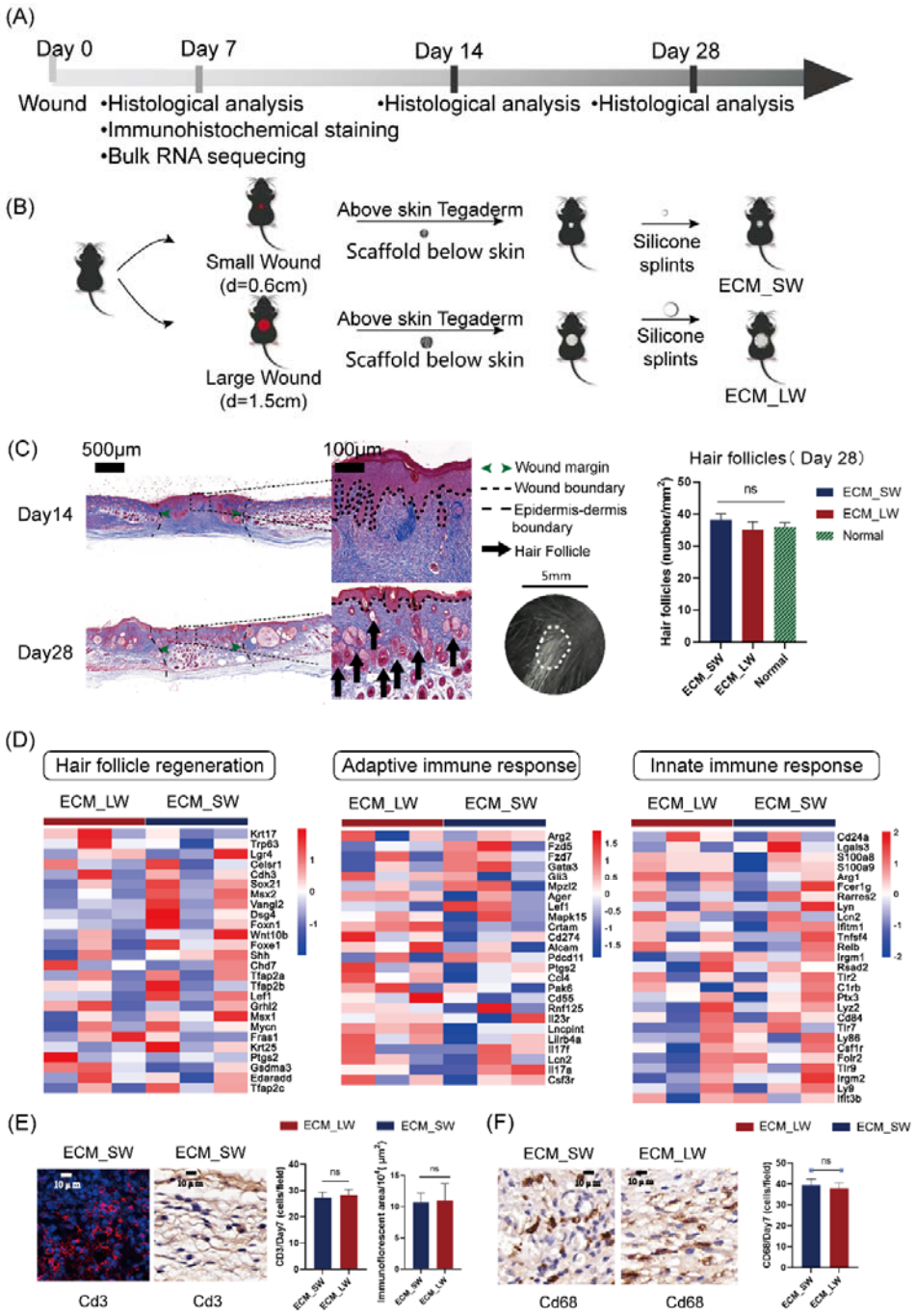

Fig.S8. Evaluation of the healing of small and large full-thickness wound with implanted ECM scaffolds. (A) Workflow for evaluating mouse skin wound healing. (B) Surgical processes for mouse skin excisional wound model. (C) Histological analysis of ECM_SW on POD

14 and POD28 and histologic quantification of de novo hair follicles on POD28. (D) Heatmap showing expression of hair follicle regeneration, adaptive immune response, and innate immune response related genes. (E) IF staining and IHC staining of Cd3 in wound center and corresponding quantification of $CD3^+$ cellular infiltration between ECM_SW and ECM_LW. (K) IHC staining of Cd68 and quantification of $CD68^+$ cellular infiltration.

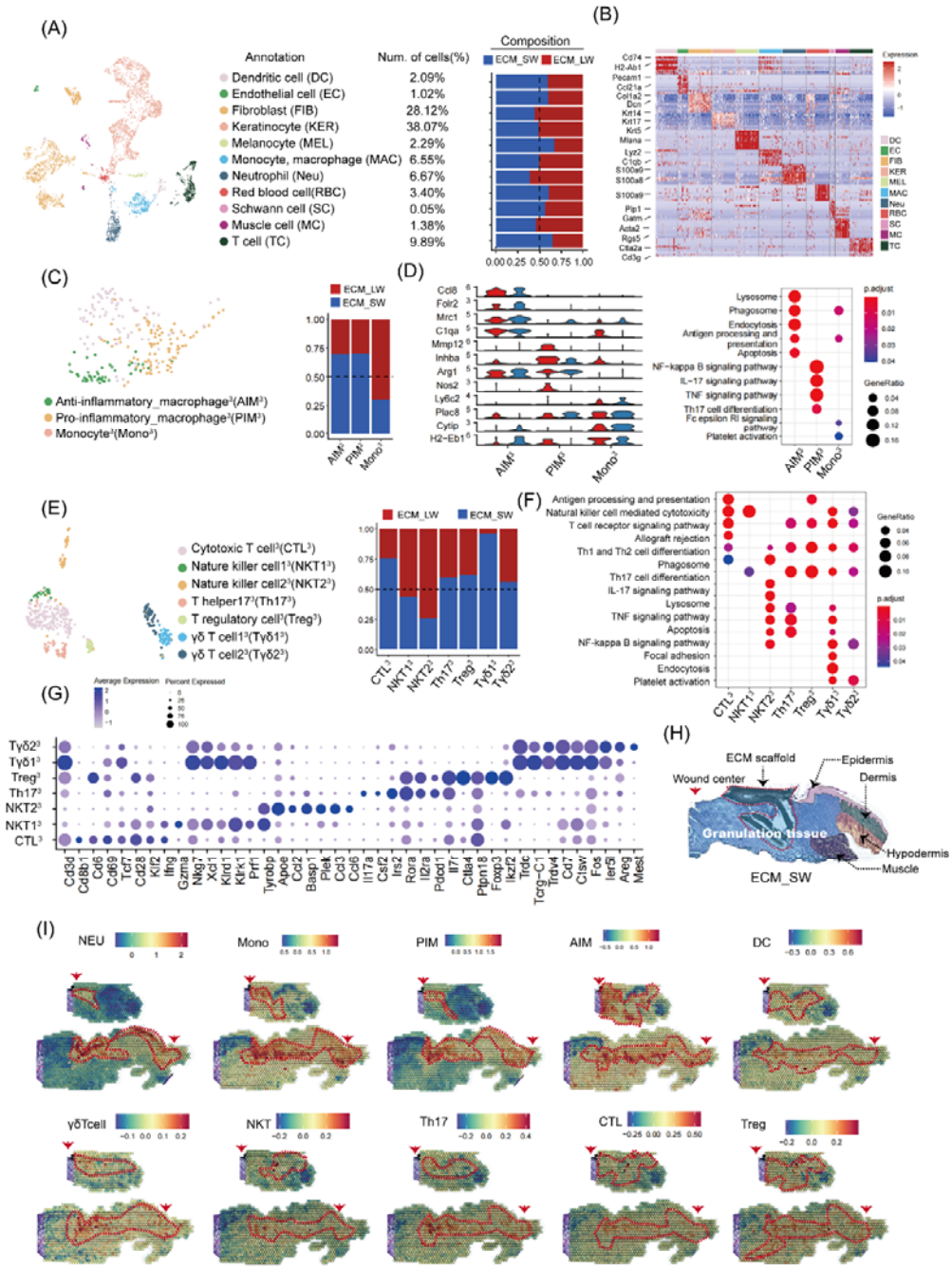

Fig. S9. Sc-RNA and ST analysis between ECM_LW and ECM_SW.

(A) Single cells were categorized into 11 main clusters. The number of cell populations in each cluster, number of cells (%), and composition of ECM_LW and Ctrl_LW groups were listed. (B) Heatmap and top10

marker genes for different clusters. (C) Subclustering of macrophages showing three subsets; The composition for each subset was listed. (D) Marker genes for each macrophage/monocyte subset and enriched gene sets in KEGG pathway analysis. (E) Subclustering of T cells showing seven subsets; The composition for each subset is listed. (F) their enriched gene sets in KEGG analysis.(G) Marker genes for T cell subsets. (H) The annotations indicated the anatomical structures of ECM_SW. (I) Spatial feature plots showed defined macrophages and T cells subclusters expression in tissue sections using Addmodulescore.